NASA
Technical
Paper
1951

November 1981

Crossflow Effects on Steady and Fluctuating Pressures on an Ogive-Cylinder Cone-Frustum Model in Supersonic Separated Flow

Jules B. Dods, Jr.,
and Charles F. Coe

NASA

NASA Technical Paper 1951

1981

Crossflow Effects on Steady and Fluctuating Pressures on an Ogive-Cylinder Cone-Frustum Model in Supersonic Separated Flow

Jules B. Dods, Jr.
Raman Aeronautics, Inc.
Palo Alto, California

Charles F. Coe
Ames Research Center
Moffett Field, California

National Aeronautics and Space Administration

Scientific and Technical Information Branch

TABLE OF CONTENTS

Page

SYMBOLS v

SUMMARY 1

INTRODUCTION 1

APPARATUS AND TECHNIQUE 2
- Wind Tunnel 2
- Description of Model and Instrumentation 2
- Test Methods 3

RESULTS AND DISCUSSION 3
- Flow Model 3
- Crossflow Effects on the Broadband Characteristics of Pressure Fluctuations 4
  - *Steady and fluctuating pressures* 4
  - *Vortex-flow characteristics* 4
  - *Effect of angle of attack* 5
  - *Effect of Reynolds number* 5
- Crossflow Effects on the Power Spectral Densities of Pressure Fluctuations 5
  - *Basic power spectral densities* 5
  - *Vortex-flow characteristics* 6
  - *Effect of angle of attack* 6
  - *Effect of Reynolds number* 7

CONCLUDING REMARKS 7

REFERENCES 8

TABLES 9

FIGURES 13

SYMBOLS

C_p static pressure coefficient, $(p - p_\infty)/q_\infty$

d body diameter, m

dB overall sound pressure level (ref. 0.0002 dynes/cm^2)

dc direct current or steady-state value, V

f frequency, Hz

$G(f)$ power spectral density function, (N/m^2)^2/Hz

h height of cone frustum and axisymmetric ring, m

ℓ_N body nose length, m

ℓ_R axisymmetric ring length (fig. 1), m

M Mach number

p static pressure, N/m^2

$\tilde{p}(x,t)$ pressure fluctuation, N/m^2

$\sqrt{\overline{\tilde{p}^2}}/q_\infty$ root-mean-square (rms) pressure coefficient

q dynamic pressure, N/m^2

Re_d Reynolds number based on d, $(\rho U_\infty d)/\mu$

s circumferential distance measured from leeward generator (fig. 6)

s/d circumferential distance in body diameters

t time, sec

U velocity along tunnel longitudinal axis, m/sec

x longitudinal distance measured from leading edge of cylinder (fig. 1), m

x/d longitudinal distance in body diameters

α angle of attack, deg

β angle of sideslip, deg

δ boundary-layer thickness at $x/d = 3.30$

θ angle of cone frustum (or flare), deg

μ free-stream viscosity of air, Nsec/m^2

ρ free-stream density of air, Nsec^2/m^4

ϕ circumferential angle around cylinder surface measured from windward generator, deg (see figs. 5 and 6)

Subscripts and superscripts:

$(\bar{\ })$ time-average of parameter under consideration

d based on body diameter

N body nose

$\tilde{p}$ fluctuating pressure

R axisymmetric ring

∞ free stream

CROSSFLOW EFFECTS ON STEADY AND FLUCTUATING PRESSURES ON AN OGIVE-CYLINDER CONE-FRUSTUM MODEL IN SUPERSONIC SEPARATED FLOW

Jules B. Dods, Jr.,* and Charles F. Coe

Ames Research Center

A wind-tunnel investigation was conducted to study the crossflow effects on the surface-pressure fluctuations underlying attached and separated turbulent boundary layers, shock waves, and vortex-type flows. An ogive-cylinder model, with protuberances consisting of 45° and 23° cone frustums and axisymmetric rings to generate the flow regions of interest, was used. The tests were made at a free-stream Mach number of 2.0 and at Reynolds numbers of 1.5×10^6 and 3.9×10^6, based on the body diameter and free-stream conditions. This investigation was conducted at angles of attack up to 8° to induce crossflow effects ($U_\infty \sin \alpha$) that produce vortex flows. The major interest was in measuring the intensity and spectral characteristics around or in the neighborhood of the foci of the vortex flows.

The results of the measurements showed that the pressure fluctuations in the vortex flows were not excessively large; in fact, they had broadband levels of the rms pressure coefficients and power spectral density characteristics that were nearly identical to those previously measured in other separated-flow regions without crossflow effects. A more significant effect of angle of attack, however, was found in the shock-wave and separated-flow regions that occur on the windward side of the model in which there were no observable vortex flows. In the shock-wave case the rms pressure coefficient increased as much as 184% at the highest angle of attack (8°); in the separated-flow region the increase was 109%. Significant changes in the power spectra, or frequency-dependent, characteristics due to angle of attack were also found in the shock-wave and the separated-flow regions. The effects of variations in Reynolds number were found to be small.

The pressure fluctuations in regions of turbulent attached flow, shock waves, and separated flow near the surfaces of aerospace vehicles result in excitations and vibrations of the structure. These inputs are important in determining stress, the fatigue life of the structure, and noise transmission into the interior of the vehicle. Therefore, a research program has been undertaken at Ames Research Center to investigate the random pressure fluctuations underlying these flow fields. The objective was to develop a data base of necessary information, including empirical expressions, that could be used to obtain preliminary estimates of the statistical characteristics of the pressure fluctuations. To carry out this research, many aspects of the problem have been investigated, including Reynolds number effects, parameters for frequency scaling, wind-tunnel background noise effects, and transducer installation and size effects. The results of most of these investigations have been reported in references 1 through 8. Additional references and a bibliography are given in reference 1.

The previously reported results have been for axisymmetric and two-dimensional flow. The axisymmetric-flow data were obtained on an ogive-cylinder model (figs. 1, 2) which included axisymmetric rings of various heights and cone frustums with angles from 15° to 90°. Using this same model, oil-flow visualization studies were made at finite angles of attack, which showed the existence of vortex flows in the regions aft of the detached frustum shock on the leeward side of the model.

The present investigation was undertaken to compare the pressure fluctuations in these various asymmetric flow regions with those previously measured when the crossflow component ($U_\infty \sin \alpha$) was zero. The tests were conducted at a free-stream Mach number of 2 and at two Reynolds numbers:

*Staff Engineer, Raman Aeronautics, Inc., Palo Alto, Calif. 94301.

($Re_d \cong 1.5 \times 10^6$ and 3.9×10^6). The ogive-cylinder model was tested with two protuberances (cone frustums and axisymmetric rings) with cone angles of 45° and 23°. The protuberances were used to generate detached shock waves and separated-flow regions ahead of the protuberance. Preliminary oil-flow visualization studies were used to select the tunnel parameters and model attitudes, and to select the pressure transducer locations for the detailed pressure measurements.

The report presents both the steady-state and fluctuating static-pressure measurements. The fluctuating pressures are given in terms of the broadband (rms) characteristics, and typical power spectral densities ($G(f)$) are also illustrated. The effects of changes in the Reynolds number on the pressures are also presented.

APPARATUS AND TECHNIQUE

Wind Tunnel

The 9- by 7-Foot Supersonic Wind Tunnel at Ames Research Center was used for all tests. This wind tunnel, which is a closed-circuit type, has a continuously variable Mach number range from 1.5 to 2.6, with a Reynolds number capability from 0.5×10^6 to 2.0×10^6/m.

The environmental noise in the 9- by 7-Foot Wind Tunnel was measured in the study reported in reference 5. For the conditions of the present tests, the overall sound pressure levels varied from 122 to 132 dB, which corresponds to an rms pressure coefficient, $\sqrt{\tilde{p}^2}/q_\infty$, of about 0.0015. Since the wind tunnel has solid walls, there are no discrete edge tones in the flow. However, a small disturbance occurs at approximately 1,000 Hz because of impulses imparted to the stream from the 11-stage compressor. The disturbance can only be seen in the power spectra of pressure fluctuations from attached boundary layers, and it is completely obscured by the larger pressure fluctuations that are characteristic of shock waves, vortex flows, and separated-flow regions. All of the tests of the present investigation were conducted at a free-stream Mach number of 2 at Reynolds numbers (Re_d, based on model diameter) of 1.5×10^6 and 3.9×10^6. Further details of the tunnel characteristics may be found in reference 9.

Description of Model and Instrumentation

Sketches of the ogive-cylinder model used for the investigation and typical flow regions over the model are shown in figure 1. The model is shown installed in the wind tunnel in figure 2. The basic diameter of the model was 0.254 m. The cylindrical section of the model was 8.30 diam in length, and the ogive nose was 3.00 diam in length. Cone frustums ahead of axisymmetric rings were added to the cylinder to generate the flow regions of interest. The leading edges of the frustums were always positioned at an x/d of 4.00; they had the angles, heights, and lengths shown in figure 1. The boundary layer was tripped by the grit strip located near the nose of the model. The thickness of the attached boundary layer, used to nondimensionalize the pressure fluctuations, varied from approximately 0.0166 m at the lower test Re_d to 0.0154 m at the higher Re_d at x/d = 3.30. The thickness was measured with a boundary-layer rake on the clean body at four longitudinal stations, and the resulting rate of change of thickness with longitudinal distance, $d\delta/dx$, was used to extrapolate the boundary-layer thickness to an x/d of 3.30. The boundary layer at this location is a reference value, immediately ahead of the detached shock wave.

The pressure instrumentation consisted of 60 static-pressure orifices and 60 dynamic-pressure transducers located on a cylindrical panel (figs. 3, 4). The longitudinal dimensions are as shown in figure 3, but the s/d, or circumferential dimensions are a function of ϕ, the angle around the cylinder surface; they are shown in table 1. A sketch of the model mounted in the wind tunnel is shown in figure 5; it illustrates the various angular directions and clarifies the definition of ϕ, which is referenced to the centerline of the instrumented surface panel. To assess the extent of the vortex-flow region and to maintain a reasonably concentrated array of transducers to adequately define the flow, the instrumented panel was rolled through the flow field to several discrete values of ϕ, and the data point was repeated. Because the model is a body of revolution, measurements at any ϕ were obtained with the same instrumentation by rotating the model about its longitudinal axis. The steady-state pressures were measured using standard multiport Scanivalve instrumentation and a digital recorder. The internal diameter of the static orifices was 0.00056 m. The fluctuating pressures were measured with

semiconductor-type Kulite pressure transducers having a sensing diameter of 0.00121 m. The transducers were mounted nearly flush (2.5×10^{-5} m below the surface), as recommended in reference 8. They were individually powered by dc voltage supplies. The output signals were amplified by automatic gain-ranging amplifiers and were recorded with a frequency range using high-pass filtering from 3 Hz to 20 kHz on two FM 32-channel Ampex FR-1800 tape recorders at a tape speed of 60 ips.

The broadband dynamic signals were read by rms modules for each data channel. A scanner and a digital voltmeter (DVM) were interfaced with a Hewlett-Packard 9830 computer, which processed the signals and stored the final results on a cassette for printing and plotting. The power- and cross-power spectral densities in the frequency range from 10 Hz to 20 kHz were obtained through the use of a hybrid analog-digital computer system described in reference 7.

The model contained oil supply tubes and orifices to provide for fluorescent-oil studies of the flow. The orifices surrounded the cylinder at a longitudinal station of x/d = 2.4 with a circumferential spacing of s/d = 0.1 to give an even dispersion of the oil on the model surface.

Test Methods

The tests were conducted in two phases: phase 1 was for surface oil-flow visualization prior to installation of the pressure instrumentation; and phase 2 included the tests of the fully instrumented model for the purpose of measuring the steady and fluctuating pressures. For both phases, tests were conducted at M_∞ = 2.0 and at tunnel stagnation pressures of 50.8×10^3 and 152.4×10^3 N/m^2, which resulted in values of Re_d of about 1.5×10^6 and 3.9×10^6. The angles of attack were 0°, 4°, and 8°. The angle of sideslip was not varied from 0° (nominally 0.15°).

Fluorescent oil was used for the surface oil-flow visualization; still and motion picture cameras were used to make photographic records at each test condition. The angle of attack was varied in 4° steps from -8° to +8° for the still photographs and continuously from -8° to +8° for the motion pictures. Before taking each set of photographic data, oil was momentarily ejected onto the model surface and the flow was allowed to stabilize. Oil-flow control valves were off during still picture taking, but they were occasionally opened briefly to replenish the oil for the "α-sweep" motion pictures.

Steady-state and fluctuating pressures were measured at each of the above-mentioned test conditions with the model positioned at three values of ϕ. The ϕ settings were selected for the angle of attack used in each test so that measurements would be made in regions of vortex flows, as identified by the oil-flow tests. The ϕ increments were selected so that one longitudinal row of dynamic pressure transducers would overlap a row of transducers for the previous ϕ setting. This overlapping of measurements provided a check on the symmetry of the model and duplication of the flow field at different ϕ settings. The extent of the survey in ϕ is shown in figure 5 for the various combinations of cone-frustum angle and angle of attack. The field of view for the visual flow photographs shown in figure 6 is described in more detail in figure 7; the photographs are shown in figures 8 and 9.

RESULTS AND DISCUSSION

The discussion of crossflow effects on the steady and fluctuating pressures in supersonic flow on an ogive-cylinder model will be divided into two major categories: the broadband or rms characteristics, and the frequency-dependent or power-spectral density characteristics. In each of these categories, the discussion will be further separated into vortex-flow characteristics, the effects of angle of attack, and the effects of Reynolds number.

Flow Model

The model of the supersonic flow in a cylinder-flare junction at an angle of attack has been outlined by Ericsson et al. (ref. 10) and, more recently, explained in detail by Peake and Tobak (ref. 11). (See figures 47 and 48 in the latter document.) Numerical computations with approximate forms of the Navier-Stokes equations were published by Hung in 1979 (ref. 12).

The shock wave generated by the deflected surface of the flare interacts with the approaching boundary layer on the cylinder to form a massive zone of three-dimensional separation around the entire periphery. The most evident feature of this flow is

the pair of large spiral foci (vortices) generated ahead of the cylinder-flare junction on the leeside (see the visual-flow photographs in figs. 8 and 9). In many instances, a nonsymmetric cellular pattern is also observed at an angle of attack of 0°. Small perturbations in the free stream or in attitude may clearly trigger these asymmetric $\alpha = 0°$, $\beta = 0°$ flows.

In this report, the surface oil-flow visualization photographs illustrate patterns of skin-friction lines, from which the various singular points could be identified. For the present investigation, the primary interest was in surveying the indicated foci (vortical flow) with a mesh of fluctuating pressure instrumentation that was fine enough to permit a comparison of the fluctuating pressures around or in the neighborhood of the foci with those previously measured in other separated-flow regions without crossflow effects. A further description of the intricacies of the flow structure relating to crossflows is contained in reference 11.

In the following discussion and in some of the figures, the "other separated flow regimes without crossflow effects" will be referred to simply as "separated" flows. The separated flows identifiable as containing the larger scale vortex motion will be referred to as "vortex" or "vortical" flows.

Crossflow Effects on Broadband Characteristics of Pressure Fluctuations

Steady and fluctuating pressures– The data obtained during the investigation of the pressure fluctuations are presented in figures 8(a) through 8(l) for the ogive-cylinder model having the $\theta = 45°$ protuberance, and in figures 9(a) through 9(l) for the $\theta = 23°$ protuberance. All tests were made at $M_\infty = 2$. The steady-state pressures are presented along with the fluctuating pressures for each angle of attack and Reynolds number. The data are presented for the various rows of orifices and transducers on the unwrapped cylinder surface in an isometric view. A sketch showing the extent of the pressure instrumentation in the circumferential direction (s/d) is included for each test condition; leeward and windward views of the model, showing the corresponding flow conditions from the visual oil-flow studies, are also included (see, again, fig. 7). For an angle of attack of 0°, only the data at one set of values of ϕ are presented since the circumferential flow is symmetrical. Also, for the angular positions where the rows of transducers overlap, only one set of data is included. Several comparisons of the data from the overlapping rows indicated that the data were essentially the same.

The visual-flow photographs illustrate the vortex-flow formations at $\alpha = 4°$ and 8° that develop on the leeside of the model, as well as their absence on the windward side. Comparisons of the photographs for the two Reynolds numbers of the tests show very similar vortex patterns (see, e.g., figure pairs 8(c) and 8(i) and 8(e) and 8(k) for the $\theta = 45°$ cone frustum and 9(c) and 9(i) and 9(e) and 9(k) for the 23° cone frustum).

Vortex-flow characteristics– To compare the broadband (rms) characteristics of the fluctuating pressures in a vortical-flow region with those in a detached frustum shock and in the separated-flow region, data were selected from figures 8 and 9 and replotted in figures 10 and 11. Figure 10(a) compares the vortex flows for $\theta = 45°$ at $\alpha = 4°$ and $s/d = -0.43$ with the separated flow aft of the detached frustum shock wave at $\alpha = 0°$. It is seen here that the vortex flow fluctuating pressures are only slightly larger than those of the separated flow region. If the comparison is made for equal angles ($\alpha = 4°$), the separated flow region aft of the detached frustum shock on the windward side of the model ($s/d = -1.14$) is seen to have slightly larger fluctuating pressures than the vortex-flow region. A similar comparison is made in figure 10(b) for $\alpha = 8°$, with the same results prevailing. The overall levels, however, are somewhat larger at $\alpha = 8°$ for both the vortex-flow and the separated-flow regions than those at $\alpha = 4°$.

Comparable data are presented in figures 11(a) and 11(b) for the model with the $\theta = 23°$ cone frustum. For this configuration the pressures in the vortex-flow region at $\alpha = 4°$ (fig. 11(a)) are smaller than those in the separated flow aft of the detached frustum shock near a vortex; they are also smaller than those in the $\alpha = 0°$ separated-flow area. For the comparison at $\alpha = 8°$ (fig. 11(b)), the pressures in the vortex-flow region are smaller than those in the $\alpha = 0°$ separated flow area. For the comparison at $\alpha = 8°$ (fig. 11(b)), the pressures in the vortex-flow region are smaller than those in the $\alpha = 0°$ separated-flow area. A comparison with the pressures in the separated-flow area aft of the frustum shock on the windward side cannot be made because the separation length was so small that the separated-flow area occurred downstream of the location of the pressure transducers.

Effect of angle of attack– The effects of angle of attack on the broadband, or rms, fluctuating pressure coefficients are shown in figure 12 for the model with the $\theta = 45^\circ$ cone frustum. The angle-of-attack effects are evaluated by choosing locations on the windward side of the model that are not affected by the vortex flows. At these locations, a typical attached turbulent boundary layer, a detached frustum shock wave, and a shock-separated flow region occur, much in the same manner as those flow regions that occur for all circumferential locations (s/d) at an angle of attack of 0°. Thus, similar flow regions are being compared for all angles of attack.

It is seen from figure 12 that the pressure coefficients in the attached boundary layer upstream of the shock wave show very little effect of increases in the angle of attack. However, very significant increases in the pressures occur in both the shock wave and in the separated flow. For example, the pressure coefficients are essentially doubled in value between $\alpha = 0^\circ$ and $\alpha = 8^\circ$ for both flow regions.

The angle of attack was limited to 8° in this investigation because that angle was high enough to generate the surface vortex flows which were the primary area of interest.

Effect of Reynolds number– The effects of Reynolds number on the fluctuating pressure coefficients in the detached frustum shock and in the separated flow region ahead of the $\theta = 45^\circ$ cone frustum are presented in figures 13(a), 13(b), and 13(c) for angles of attack of 0°, 4°, and 8°, respectively. The circumferential positions were chosen to illustrate the Reynolds number effect in those areas having a detached frustum shock and not in the regions of vortex flow. The effect of varying the Reynolds number is minimal in the separated flow regions at all angles of attack. The separation length, as indicated by the location of the detached frustum shock, tends to be smaller at the higher value of Re_d at angles of attack of 0° and 4°, but there is very little difference at an angle of attack of 8°

Crossflow Effects on Power Spectral Densities of Pressure Fluctuations

Basic power spectral densities– As noted in reference 1, the power spectra made dimensionless by $G\tilde{p}(f)U_\infty/q_\infty{}^2\delta_O$ collapsed quite well for axisymmetric models having different scales where the static pressure differences through the shocks were about the same (see fig. 5 of ref. 1). Therefore, the spectra for this report were made dimensionless by the same factors. Note that δ in this report is equivalent to δ_O of reference 1 since they were both evaluated at $x/d = 3.30$ (which is "immediately ahead of the detached shock wave" at $\alpha = 0^\circ$, as defined in ref. 1). Average values of U_∞, q_∞, and δ for the different Reynolds numbers are given in table 2. The study of the crossflow effects as a function of frequency will be limited to the power spectral densities; the other frequency-dependent functions, such as phase angle, correlation coefficients, convection velocities, and attenuation coefficients, discussed in reference 1 are not considered here.

The basic crossflow effects on the power spectral densities are shown in figures 14–16 for the model with the $\theta = 45^\circ$ cone frustum, and in figures 17 and 18 for the 23° cone frustum. The data are for Reynolds numbers of approximately 1.5×10^6 and 3.9×10^6 and for angles of attack of 0°, 4°, and 8°, except that for the 23° cone frustum the data are available only at the higher Re_d for $\alpha = 4^\circ$ and 8°. Consequently, the data for both angles of attack are presented together in figure 18. With the exception of the vortex-flow region (discussed later), the data presented in figures 14–18 are considered to be "basic" in the sense that they represent the power spectral densities for all of the various flow regions (attached turbulent boundary layer, shock wave, and separated flow) for the various crossflows considered. A discussion of the differences in the spectra for the various flow regions has been presented for a two-dimensional model in figure 6 of reference 1. Generally, the observations are also valid for the axisymmetric model spectra presented here and, although the spectra change with increasing angle of attack, the characteristic shapes of the spectra in the various flow regions do not differ appreciably. The curves show the distinct differences in shapes and mean-square amplitudes that distinguish separated-flow spectra from spectra measured in regions of the nearby shock wave and of the attached turbulent boundary layer. Shock spectra are characterized by a very steep slope starting at relatively low values of the dimensionless frequency parameter, $f\delta/U_\infty$, from 3×10^{-3} to 6×10^{-3}, with high intensities at low frequencies. The first spectral data point corresponds to 10 Hz. The separated-flow spectra were at least one decade lower than the shock spectra at low frequencies. Having a less steep slope, however,

the separated-flow spectra crossed the shock spectra and had the larger spectral intensities at intermediate and high frequencies. The power spectra of the pressure fluctuations beneath the attached boundary layer were more than two decades lower than the separated-flow spectra at low frequencies for the $\theta = 45^\circ$ cone frustum, but were more of the order of one decade for the $\theta = 23^\circ$ cone frustum. Although all the spectra appear to be converging toward a common level and slope at the higher frequencies, there was still about a one-decade difference between the attached-flow and separated-flow spectra at the highest frequencies (20 kHz), except, again, the increment for the $\theta = 23^\circ$ cone frustum at angle of attack tends to be less than the one decade. The sharp peak in the spectra for the attached boundary layer occurs at a frequency of 1 kHz and is attributable to the blade-passing frequency imparted to the airstream by the 11-stage compressor of the wind tunnel; therefore, it is not a characteristic of the boundary layer .

Although the rms pressure coefficients were discussed in the first portion of this report, the broadband pressure coefficients for the individual power spectra given in figures 14–18 are also given in table 3 for reference. These pressure coefficients are obtained by integrating the power spectra, a procedure theoretically equivalent to the method for obtaining the rms pressure coefficients presented in figures 8–13, using the rms modules and associated equipment described in a previous section (Description of Model and Instrumentation). These two procedures have also been shown to be equivalent experimentally within acceptable limits. The percentage differences in the integrated pressure coefficients shown in table 3 illustrate the large variation in intensities between the various flow regions. The values for the attached turbulent boundary layer are used as a base value in computing the percentage differences.

Vortex-flow characteristics– The spectral characteristics of vortex-flow regions for the model with the $\theta = 45^\circ$ cone frustum are presented in figure 19 for "small" crossflows ($\alpha = 4^\circ$) and in figure 20 for "large" crossflows ($\alpha = 8^\circ$), for the two values of Reynolds number tested. The data are for various longitudinal positions through a vortex beginning at $x/d = 3.25$ and extending to $x/d = 3.95$. At $\alpha = 4^\circ$, the first longitudinal spectrum has the characteristic shape of a shock wave, suggesting that there is a small shock preceding the vortex formation. The remaining spectra have basically similar shapes with intensities increasing in the downstream direction. These spectral shapes are very similar to the separated-flow spectra (compare fig. 19 with fig. 15). At $\alpha = 8^\circ$ (fig. 20), all of the longitudinal spectra appear to be due to vortex flows with no interference from shock waves. These spectra also are similar to the separated-flow spectra in figure 16.

For the $\theta = 23^\circ$ cone frustum, the data at $\alpha = 4^\circ$ and 8° were taken only for one Reynolds number. The vortex spectra were therefore combined with the spectra of the other flow regions for convenience; they are presented in figure 18. Here, again, the vortex-flow spectra are very similar to the separated-flow spectra at $\alpha = 4^\circ$. A suitable separated-flow spectra for $\alpha = 8^\circ$ was not available for comparison because the detached shock wave on the windward side of the model was so near the cone frustum that no measurements were obtained in the separated-flow region.

A summary of the integrated rms pressure coefficients for the vortex-flow power spectra is presented in table 4. In considering the percentage differences listed there, the spectrum from the upstream location is used as a base. For $\alpha = 8^\circ$, the integrated spectral intensities, which are equivalent to the broadband rms intensities, increase markedly as one proceeds in a downstream direction. For $\alpha = 4^\circ$, the intensities also increase in the downstream direction, but by a considerably smaller rate. This fact is not apparent from the percentage difference values listed for $\alpha = 4^\circ$ in table 4 because the base value at $x/d = 3.25$ was, as previously mentioned, influenced by a shock wave; as a result, it has a larger intensity than would be expected for a purely vortex flow. If the base value is ignored, an inspection of the actual values of the pressure coefficients of the remaining spectra shows that the intensities do increase as stated above.

Effect of angle of attack– The effects of angle of attack on the spectral characteristics of the pressure fluctuations of the model with the $\theta = 45^\circ$ cone frustum are presented in figures 21–23, and for the $\theta = 23^\circ$ cone frustum in figure 24. The data are presented for the attached turbulent boundary layer, for the shock wave, and for the separated-flow regions for both values of the Reynolds number considered for $\theta = 45^\circ$. The data at angles of attack for the $\theta = 23^\circ$ cone frustum are available only at the higher Reynolds number and only for the attached turbulent boundary layer.

The integrated rms pressure coefficients for the power spectra in figures 21-24 are summarized in table 5. The percentage differences are computed using the values at $\alpha = 0^\circ$ as a base. The spectral shapes for the various angles of attack for $\theta = 45^\circ$ for the attached boundary layer were not appreciably changed as the angle of attack was increased (figs. 21(a), 21(b)). (Note that the data for the attached-flow case at $\alpha = 4^\circ$ for lower Re_d (fig. 21(a)) are not available.) At the higher Reynolds number, however (fig. 21(b)), the spectral shapes for all angles of attack for the attached turbulent boundary layer are similar, and the integrated pressure coefficients decrease moderately (from 12 to 23%) with increasing angle of attack. A similar decrease (8 to 20%) was measured for the $\theta = 23^\circ$ cone frustum (see fig. 24 and table 5). The decrease in the intensity of the pressure fluctuations may be caused by a thinning of the boundary layer on the windward side of the model as angle of attack is increased.

The shock-wave spectra shown in figures 22(a) and 22(b) for the $\theta = 45^\circ$ cone frustum show that the effect of increasing the angle of attack was to increase (1) the frequency at which the characteristic sharp reduction in the intensity occurred, (2) the slope of the curve, and (3) the overall levels by a considerable amount (163 to 184%) (table 5).

The effect of angle of attack on the separated-flow spectra in figures 23(a) and 23(b) was to increase the intensity in the low-frequency range of $f\delta/U_\infty \cong 1 \times 10^{-2}$ at $\alpha = 4^\circ$ and at about $f\delta/U_\infty \cong 1.5 \times 10^{-2}$ at $\alpha = 8^\circ$, and also in the higher frequencies ranging from $f\delta/U_\infty \cong 1 \times 10^{-1}$ to the frequency limit of the analysis of $f\delta/U_\infty = 6 \times 10^{-1}$. As shown in table 5, these increases resulted in increases of 50 to 109% in the broadband, or rms, pressure coefficients.

Effect of Reynolds number– The effects of Reynolds number on the power spectra of the pressure fluctuations are presented in figures 25 and 26 for the model with the $\theta = 45^\circ$ cone frustum and in figure 27 for the $\theta = 23^\circ$ cone frustum. The integrated rms pressure coefficients are listed in table 6 for the two values of Reynolds number tested. The percentage differences in these values are also given, using the value at the larger Reynolds number as a base value.

Generally, the effects of Reynolds number on either the shape of the power spectra or on the broadband intensities were small. The percentage differences fall in the range of 2 to 31%.

CONCLUDING REMARKS

As stated in the Introduction, the major reason for conducting the present study was to investigate the pressure fluctuations in the widely asymmetrical flows about an ogive-cylinder model which result from a crossflow component ($U_\infty \sin \alpha$) and from changes in the longitudinal pressure gradient at finite angles of attack. In particular, the major interest was around or in the neighborhood of the foci of the vortex flows. The results of the investigation show that the pressure fluctuations in these vortex-flow regions were not excessively large; in fact, they had broadband levels of the rms pressure coefficients and power spectral density characteristics that were nearly identical to those previously measured in other separated-flow regions without crossflow effects.

A more significant effect of angle of attack, however, was found in the shock-wave and separated-flow regions that occur on the windward side of the model in which there were no observable vortex flows. In the shock wave, the rms pressure coefficient increased as much as 184% at the highest angle of attack (8°), and in the separated-flow region the increase was 109%. Significant changes in the power spectra, or frequency-dependent, characteristics due to angle of attack were also found in both the shock-wave and the separated-flow regions. Generally, the effects of Reynolds number on either the shape of the power spectra or on the broadband intensities were small.

Ames Research Center
National Aeronautics and Space Administration
Moffett Field, California 94035, May 12, 1981

REFERENCES

1. Coe, C. F.; Chyu, W. J.; and Dods, J. B., Jr.: Pressure Fluctuations Underlying Attached and Separated Supersonic Turbulent Boundary Layers and Shock Waves. AIAA Paper 73-996, 1973.
2. Chyu, W. J.; and Hanly, R. D.: Power- and Cross-Spectra and Space-Time Correlations of Surface Fluctuating Pressures at Mach Numbers Between 1.6 and 2.5. NASA TN D-5440, 1969.
3. Coe, C. F.: Surface Pressure Fluctuations Associated with Aerodynamic Noise. In: Basic Aerodynamic Noise Research, NASA SP-207, 1969, pp. 409-424.
4. Coe, C. F.; and Chyu, W. J.: Pressure Fluctuation Inputs and Response of Panels Underlying Attached and Separated Supersonic Turbulent Boundary Layers. AGARD Symposium on Acoustic Fatigue, Toulouse, France, AGARD-CP-113, Sept. 1972.
5. Dods, J. B., Jr.; and Hanly, R. D.: Evaluation of Transonic and Supersonic Wind Tunnel Background Noise and Effects of Surface Pressure Fluctuation Measurements. AIAA Paper 72-1004, 1972.
6. Lewis, T. L.; and Dods, J. B., Jr.: Wind Tunnel Measurements of Surface-Pressure Fluctuations at Mach Numbers of 1.6, 2.0, and 2.5 Using 12 Different Transducers. NASA TN D-7087, 1972.
7. Lim, R. S.; and Cameron, W. D.: Power and Cross-Power Spectrum Analysis by Hybrid Computers. NASA TM X-1324, 1966.
8. Hanly, R. D.: Effects of Transducer Flushness on Fluctuating Surface Pressure Measurements. In: Supersonic, Attached Turbulent Boundary-Layer Flow. AIAA Paper 75-534, 1975.
9. Research Facilities Summary. Vol. II. Wind Tunnels: Subsonic, Transonic, Supersonic. NASA TM X-59257, 1965.
10. Ericsson, L. E.; Reding, J. P.; and Guenther, R. A.: Effects of Shock-Induced Separation. L-87-69-1, Lockheed Missiles and Space Co., Sunnyvale, Calif., July 1969; also NASA CR-107673.
11. Peake, D. J.; and Tobak, M.: Three-Dimensional Interactions and Vortical Flows with Emphasis on High Speeds. NASA TM-81169, 1980; also AGARDograph 252, July 1980.
12. Hung, C. M.: Numerical Solution of Supersonic Laminar Flow Over an Inclined Body of Revolution. AIAA Paper 79-1547, 1979.

TABLE 1.– COORDINATES FOR DYNAMIC TRANSDUCERS AND STATIC ORIFICES

Dynamic transducers or static orifice number					Dynamic transducers						
Row				x/d	Row	$\alpha = 4°$			$\alpha = 8°$		
						ϕ					
1 or 5	2 or 6	3 or 7	4 or 8			180°	145.5°	214.5°	270°	235.5°	304.5°
						s/d					
1	16	31	46	3.25							
2	17	32	47	3.30	1	0.15	0.45	-0.15	-0.64	-0.33	-0.94
3	18	33	48	3.35							
4	19	34	49	3.40	2	.05	.35	-.25	-.74	-.43	-1.04
5	20	35	50	3.45	3	-.05	.25	-.35	-.84	-.53	-1.14
6	21	36	51	3.50							
7	22	37	52	3.55	4	-.15	.15	.45	-.94	-.63	-1.24
8	23	38	53	3.60		Static orifices					
9	24	39	54	3.65	5	.12	.43	-.18	-.66	-.36	-.96
10	25	40	55	3.70	6	.02	.33	-.28	-.76	-.46	-1.06
11	26	41	56	3.75							
12	27	42	57	3.80	7	-.08	.23	-.38	-.86	-.56	-1.16
13	28	43	58	3.85	8	-.12	.18	-.43	-.91	-.61	-1.21
14	29	44	59	3.90							
15	30	45	60	3.95							

TABLE 2.– NONDIMENSIONALIZING FACTORS FOR POWER SPECTRAL DENSITIES

Re_d	U_∞, m/sec	q_∞, N/m^2	δ, m
1.5×10^6	531	18.179×10^3	0.0166
3.9×10^6	548	53.283×10^3	.0154

TABLE 3.– INTEGRATED ROOT-MEAN-SQUARE PRESSURE COEFFICIENTS – POWER SPECTRAL DENSITIES

Reference figure	θ, deg	Type of flow	α, deg	$Re_d \times 10^6$	x/d	s/d	$\sqrt{\bar{\tilde{p}}^2}/q_\infty$	Percent difference in $\sqrt{\bar{\tilde{p}}^2}/q_\infty$
14(a)	45	Attached	0	1.54	3.25	-0.64	0.0033	–
		Shock			3.40		.0356	978
		Separated			3.65		.0194	488
		Separated			3.95		.0212	542
14(b)		Attached		3.94	3.25	-0.84	.0026	–
		Shock			3.45		.0375	1342
		Separated			3.65		.0248	854
		Separated			3.95		.0243	835
15(a)		Attached	4	1.52	3.30	-1.24	.0042	–
		Shock			3.75		.0535	1174
		Separated			3.65		.0311	640
		Separated			3.95		.0267	536
15(b)		Attached		3.88	3.25	-1.14	.0023	–
		Shock			3.50		.0775	3270
		Separated			3.65		.0306	1230
		Separated			3.95		.0412	1691
16(a)		Attached	8	1.52	3.25	-1.24	.0024	–
		Shock			3.55		.0936	3800
		Separated			3.70		.0405	1588
		Separated			3.95		.0241	904
16(b)		Attached		3.92	3.25		.0020	–
		Shock			3.55		.1066	5230
		Separated			3.75		.0373	1765
		Separated			3.95		.0581	2805
17(a)	23	Attached	0	1.51	3.65	-0.15	.0030	–
		Shock			3.75		.0254	747
		Separated			3.80		.0177	490
17(b)		Attached		3.98	3.70		.0025	–
		Shock			3.80		.0370	1380
		Separated			3.85		.0192	668
		Separated			3.95		.0235	840
18(a)		Attached	4	~3.9	3.50	-0.05	.0023	–
		Shock			3.65		.0203	783
		Vortex			3.75		.0107	365
		Vortex			3.95		.0136	491
		Separated			3.95		.0160	596
18(b)		Attached	8		3.40	-0.74	.0020	–
		Shock			3.55		.0185	825
		Vortex			3.70		.0094	370
		Vortex			3.95		.0183	815

TABLE 4.– INTEGRATED ROOT-MEAN-SQUARE PRESSURE COEFFICIENTS – VORTEX POWER SPECTRAL DENSITIES

Reference figure	θ, deg	Type of flow	α, deg	$Re_d \times 10^6$	x/d	s/d	$\sqrt{\tilde{p}^2}/q_\infty$	Percent difference in $\sqrt{\tilde{p}^2}/q_\infty$
19(a)	45	Vortex	4	1.52	3.25	-0.64	0.0214	–
					3.45		.0208	-3
					3.65		.0244	14
					3.95		.0334	56
19(b)				3.88	3.25	-0.33	.0247	–
					3.45		.0196	-21
					3.65		.0203	-18
					3.95		.0250	1
20(a)			8	1.52	3.25	-0.74	.0162	–
					3.45		.0221	36
					3.60		.0284	75
					3.95		.0413	155
20(b)				3.92	3.25		.0143	–
					3.45		.0220	54
					3.65		.0266	58
					3.95		.0436	205

TABLE 5.– INTEGRATED ROOT-MEAN-SQUARE PRESSURE COEFFICIENTS – EFFECT OF ANGLE OF ATTACK ON POWER SPECTRAL DENSITIES

Reference figure	θ, deg	Type of flow	α, deg	$Re_d \times 10^6$	x/d	s/d	$\sqrt{\tilde{p}^2}/q_\infty$	Percent difference in $\sqrt{\tilde{p}^2}/q_\infty$
21(a)	45	Attached	0	~1.5	3.25	-0.64	0.0033	–
			4 (n.a)					– (n.a.)
			8		3.25		.0024	-27
21(b)			0	~3.9		-0.84	.0026	–
			4			-1.14	.0023	-12
			8			-1.24	.0020	-23
22(a)		Shock	0	~1.5	3.40	-0.64	.0356	–
			4		3.75	-1.24	.0535	50
			8		3.55		.0936	163
22(b)			0	~3.9	3.45	-0.84	.0375	–
			4		3.50	-1.14	.0775	107
			8		3.55	-1.24	.1066	184
23(a)		Separated	0	~1.5	3.65	-0.64	.0194	–
			4			-1.24	.0311	60
			8		3.70		.0405	109
23(b)			0	~3.9	3.65	-0.84	.0248	–
			4			-1.14	.0306	23
			8		3.75	-1.24	.0373	50
24	23	Attached	0		3.70	-0.15	.0025	–
			4		3.50	-0.05	.0023	-8
			8		3.40	-0.74	.0020	-20

TABLE 6.– INTEGRATED ROOT-MEAN-SQUARE PRESSURE COEFFICIENTS – EFFECT OF REYNOLDS NUMBER ON POWER SPECTRAL DENSITIES

Reference figure	θ, deg	Type of flow	α, deg	$Re_d \times 10^6$	x/d	s/d	$\sqrt{\tilde{p}^2}/q_\infty$	Percent difference in $\sqrt{\tilde{p}^2}/q_\infty$
25(a)	45	Attached	0	3.94	3.25	-0.84	0.0026	–
				1.54		-.64	.0033	27
		Shock		3.94	3.45	-.84	.0375	–
				1.54	3.40	-.64	.0356	-5
25(b)		Attached	4	3.88	3.25	-1.14	.0023	–
				1.52	3.30	-1.24	–	(n.a.)
		Shock		3.88	3.50	-1.14	.0775	–
				1.52	3.75	-1.24	.0535	-31
25(c)		Attached	8	3.92	3.25	-1.24	.0020	–
				1.52	3.25		.0024	20
		Shock		3.92	3.55		.1066	–
				1.52	3.55		.0936	-12
26(a)		Separated	0	3.94	3.65	-0.84	.0248	–
			0	1.54		-0.64	.0194	-22
26(b)			4	3.88		-1.14	.0306	–
			4	1.52		-1.24	.0311	2
26(c)			8	3.92	3.75		.0373	–
			8	1.52	3.70		.0405	9
27(a)	23	Attached	0	3.98	3.70	-0.15	.0025	–
				1.51	3.65		.0030	20
27(b)		Shock		3.98	3.80		.0370	–
				1.51	3.75		.0254	-31
27(c)		Separated		3.98	3.85		.0192	–
				1.51	3.80		.0177	-8

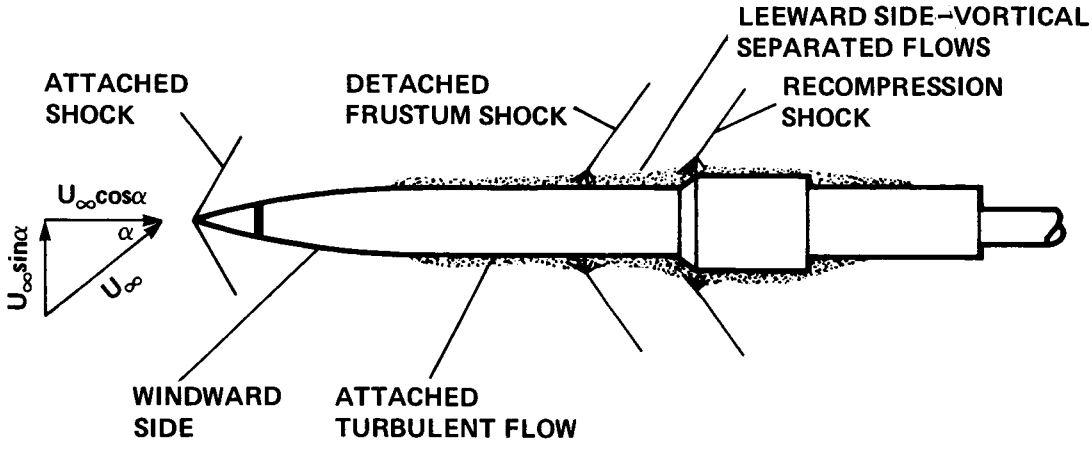

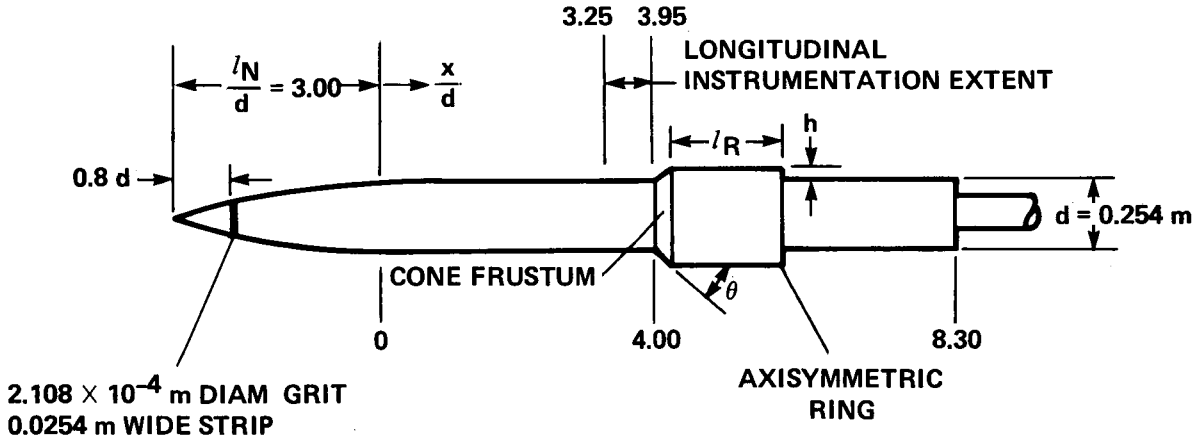

θ	h	l_R
45°	0.2d	1.6d
23°	0.3d	2.0d

Figure 1.– Description of the ogive nose cylinder model and typical flow regions over the model.

Figure 2.– Ogive-cylinder model with $\theta = 45^\circ$ cone frustum and axisymmetric ring.

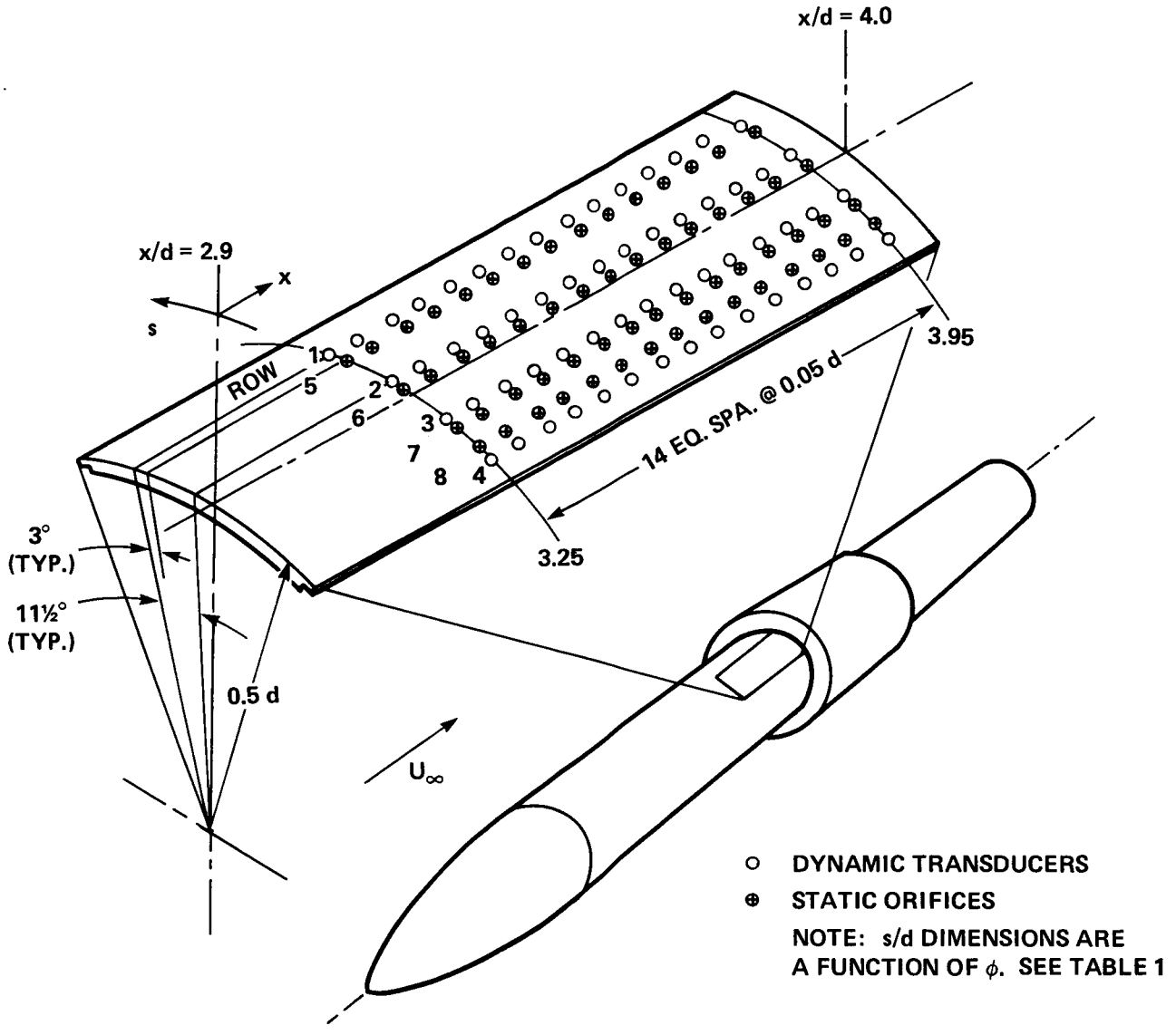

Figure 3.– Pressure-instrumentation coordinates.

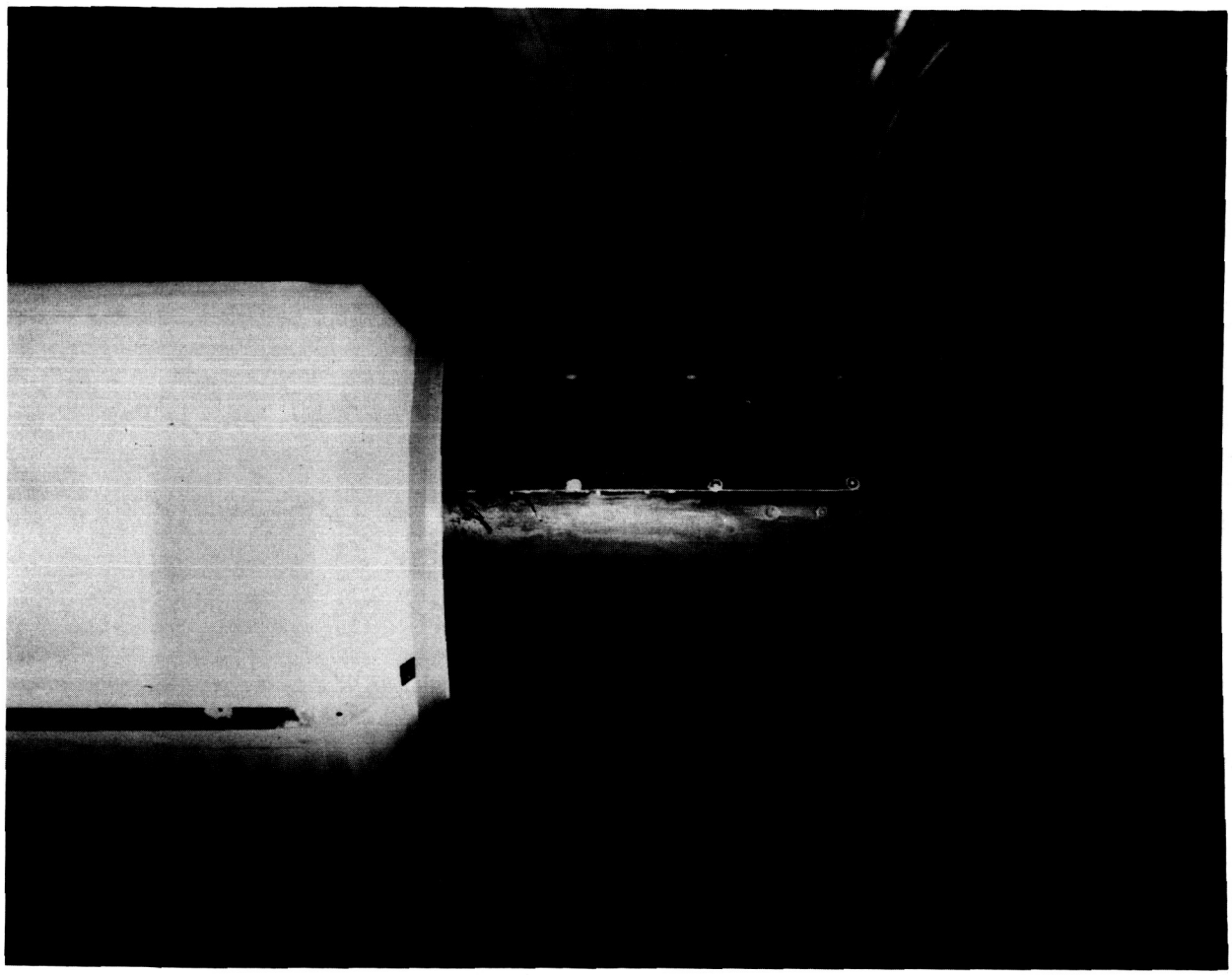

Figure 4.– Detail of instrumented panel (photo taken prior to transducer installation).

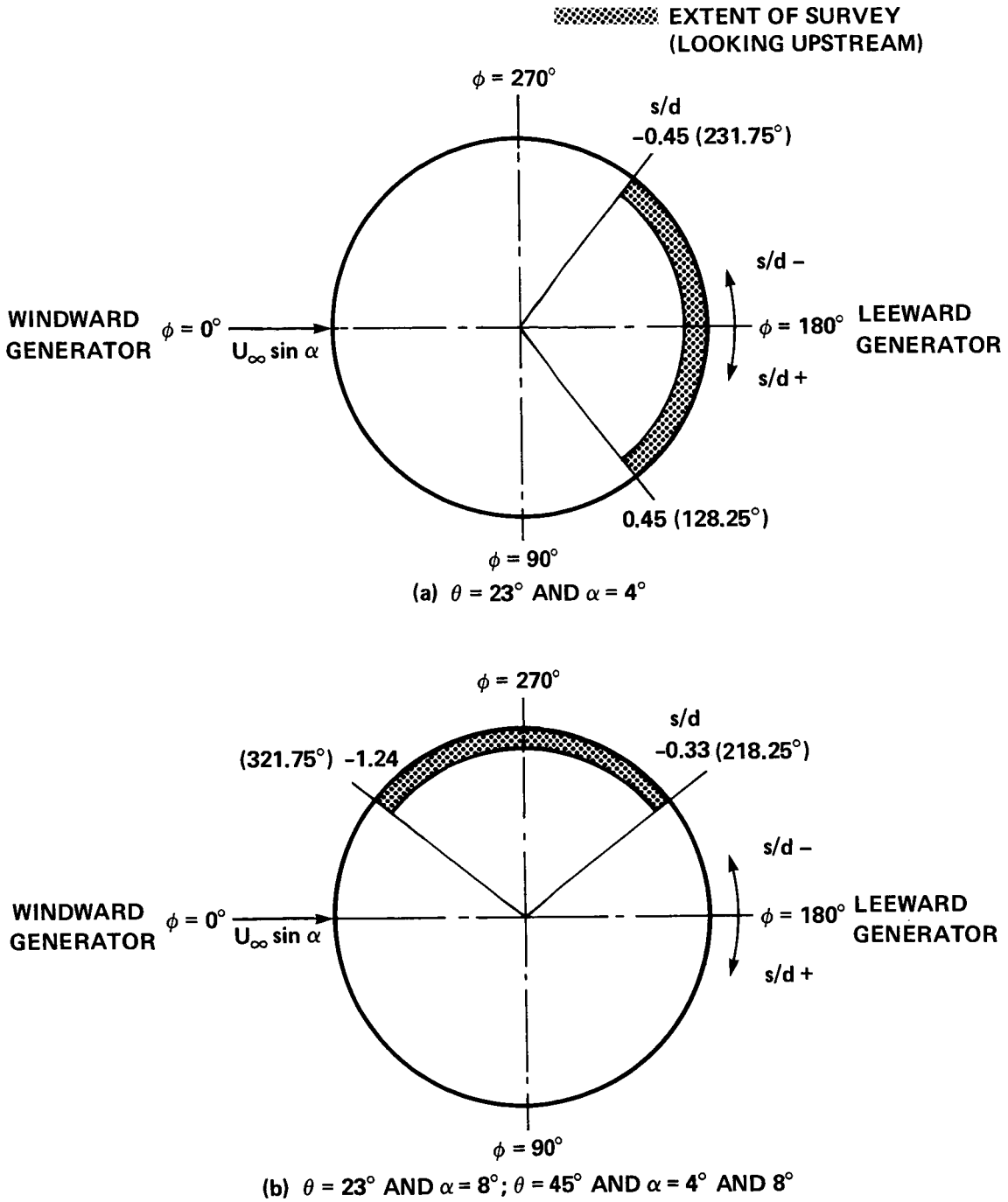

Figure 5.– Extent of the survey of the steady and fluctuating pressures on the ogive-cylinder model.

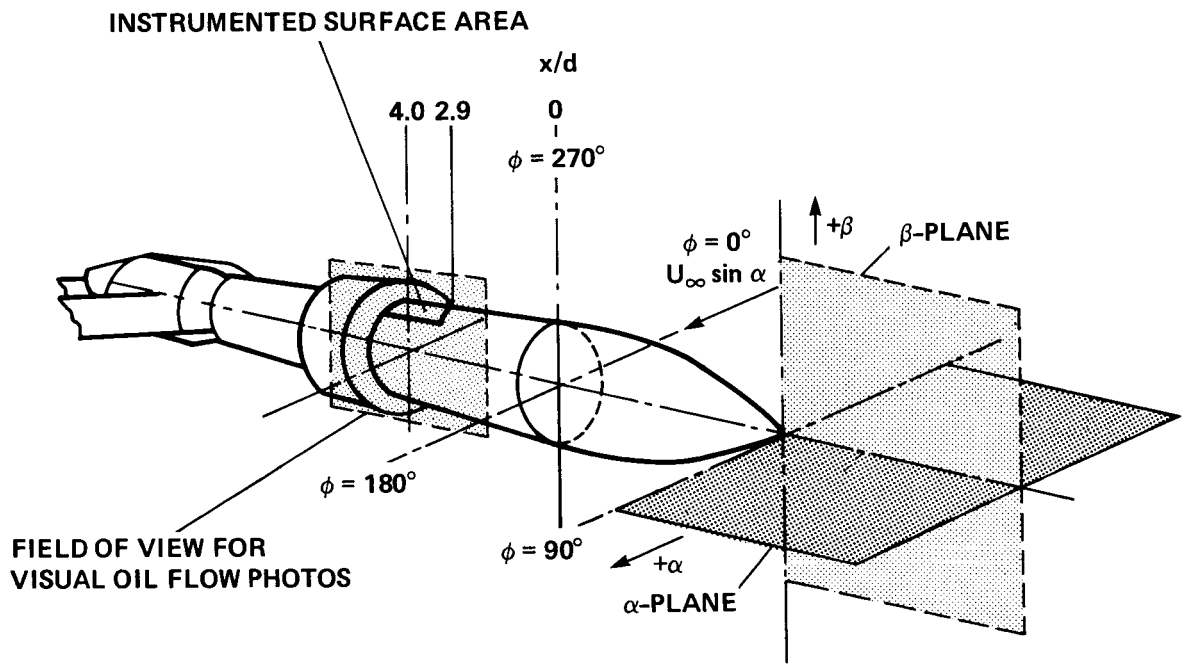

Figure 6.- Angular orientation of the model with respect to the wind tunnel.

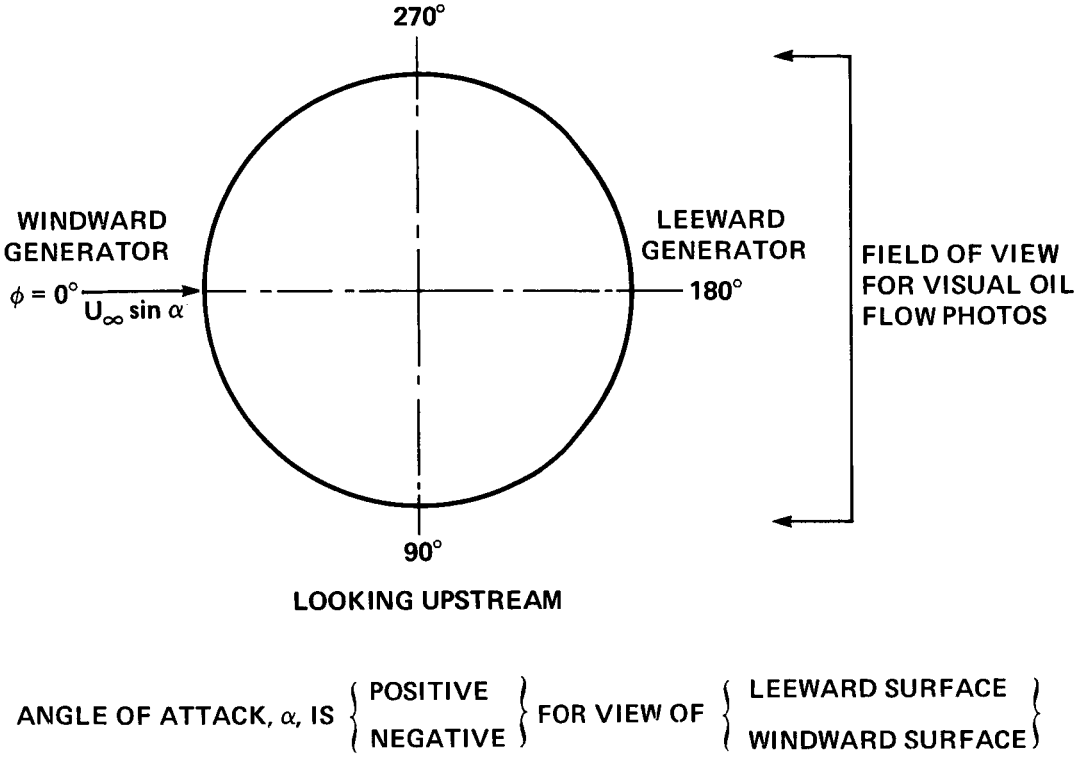

Figure 7.- Description of the field of view for visual oil flow photos of the model.

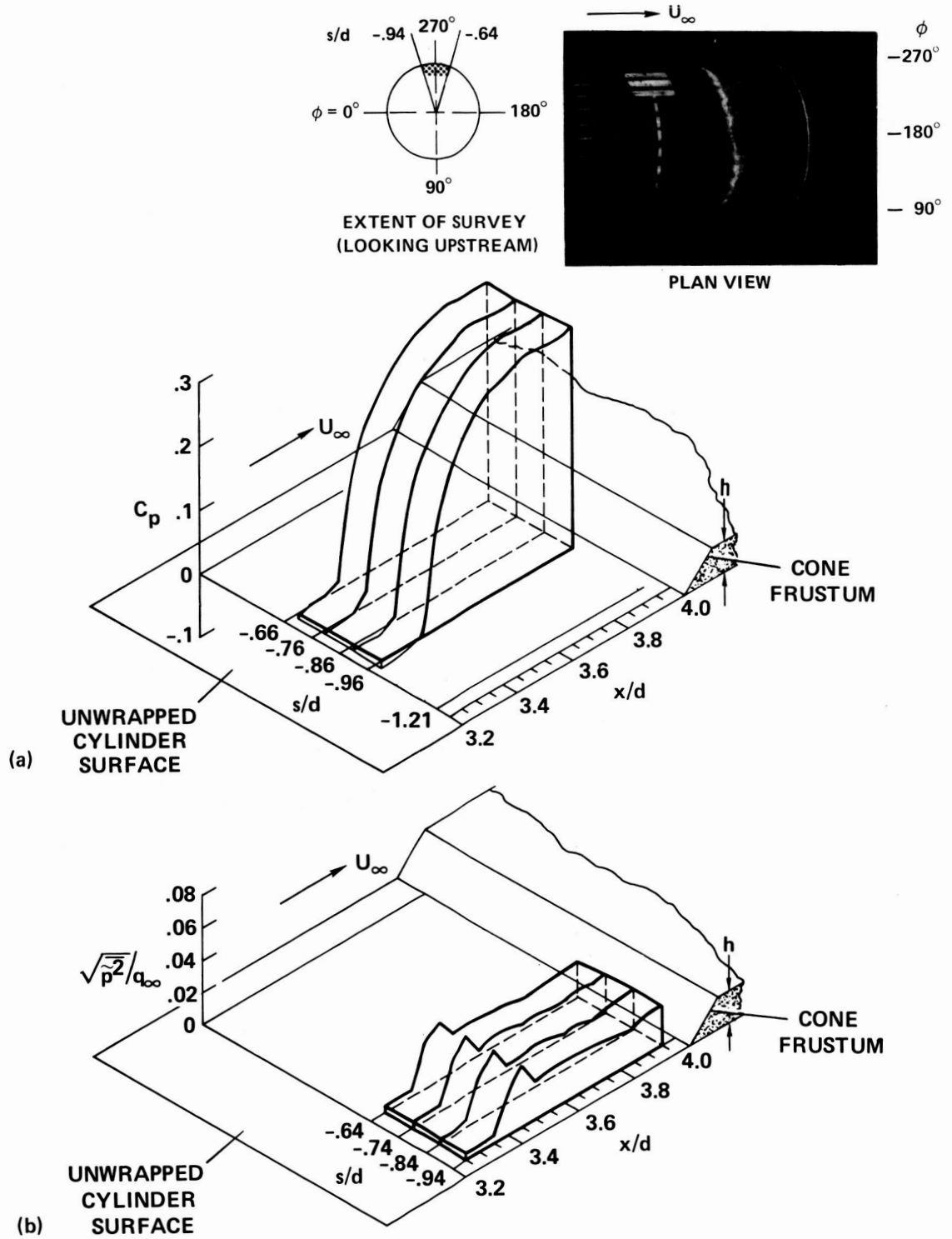

(a) Steady pressures; $\alpha = 0°$; $Re_d = 3.94 \times 10^6$.

(b) Fluctuating pressures; $\alpha = 0°$; $Re_d = 3.94 \times 10^6$.

Figure 8.– Longitudinal and circumferential variation of the steady and fluctuating pressures in the attached, shock, separated, and vortex flow regions ahead of a $\theta = 45°$ cone frustum and axisymmetric ring on the ogive-cylinder model at $M_\infty = 2.0$; $\beta = 0.2°$; $h = 0.0508$ m.

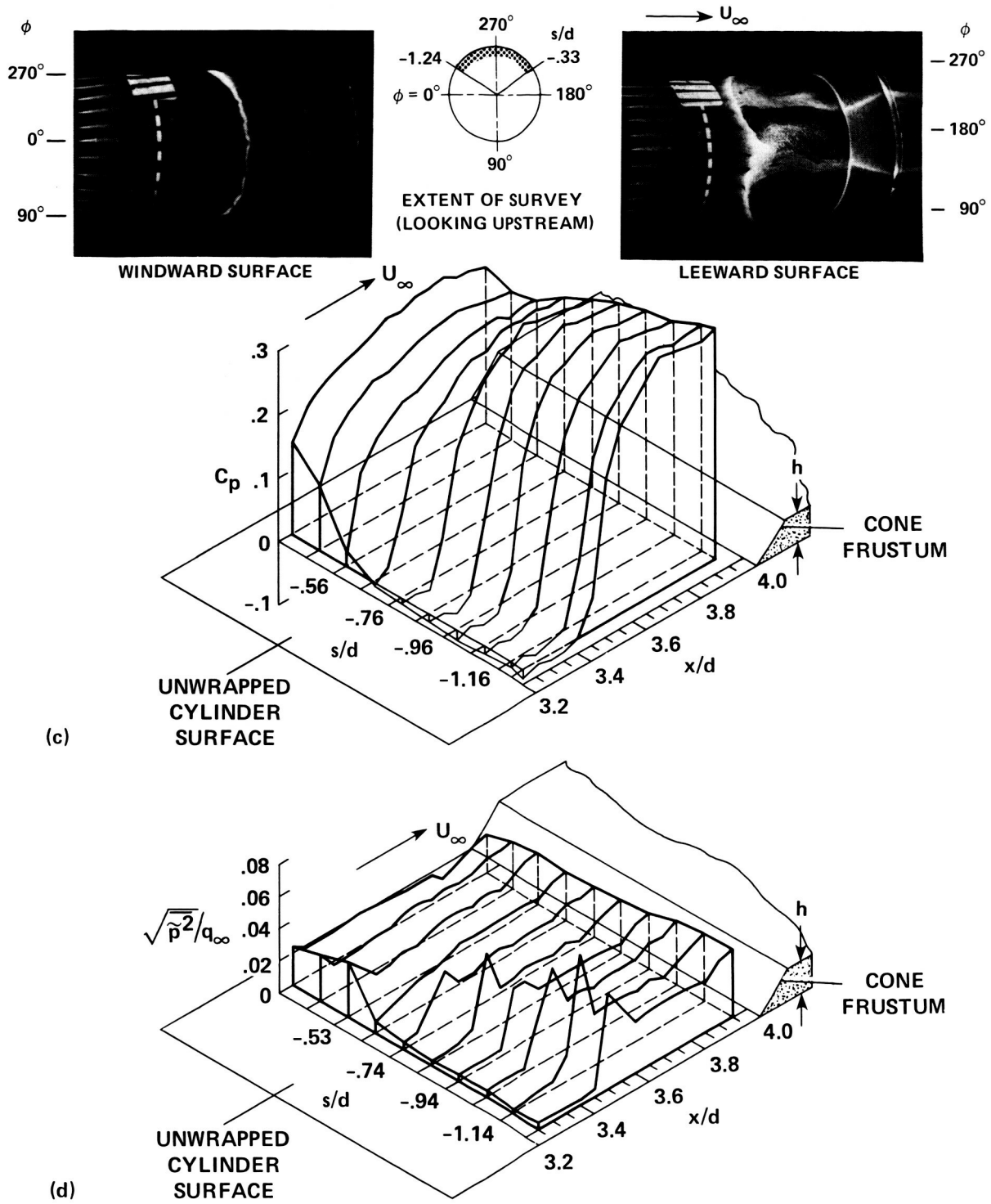

(c) Steady pressures; $\alpha = 4°$; $Re_d = 3.88 \times 10^6$.

(d) Fluctuating pressures; $\alpha = 4°$; $Re_d = 3.88 \times 10^6$.

Figure 8.– Continued.

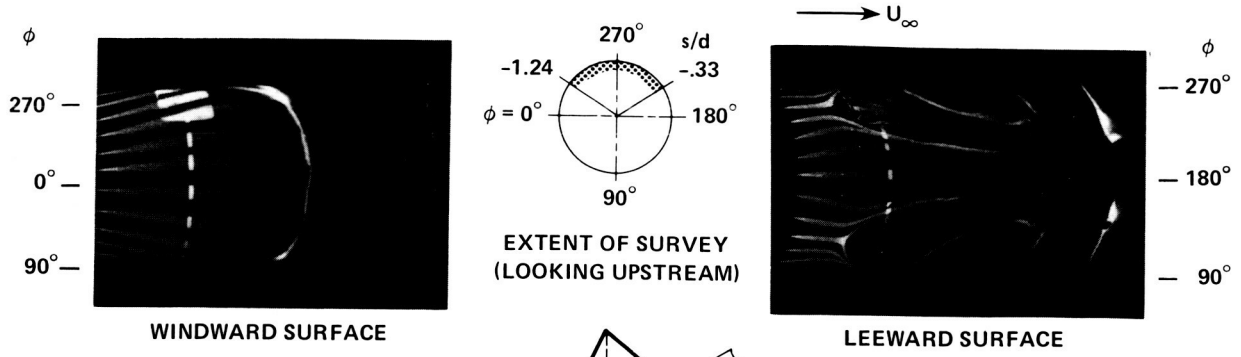

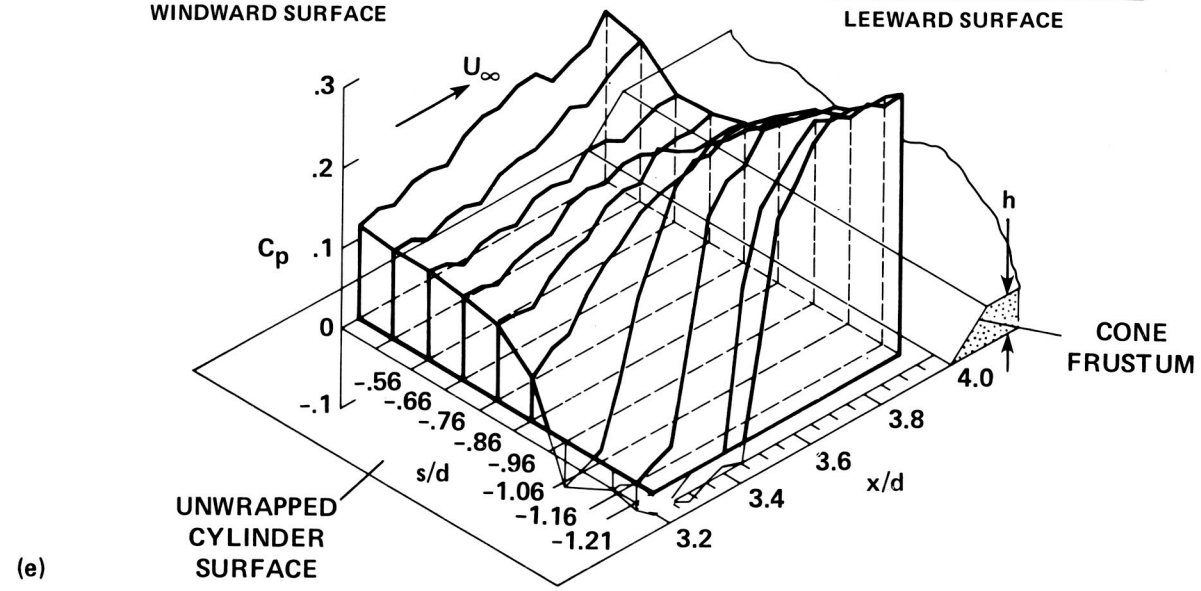

(e)

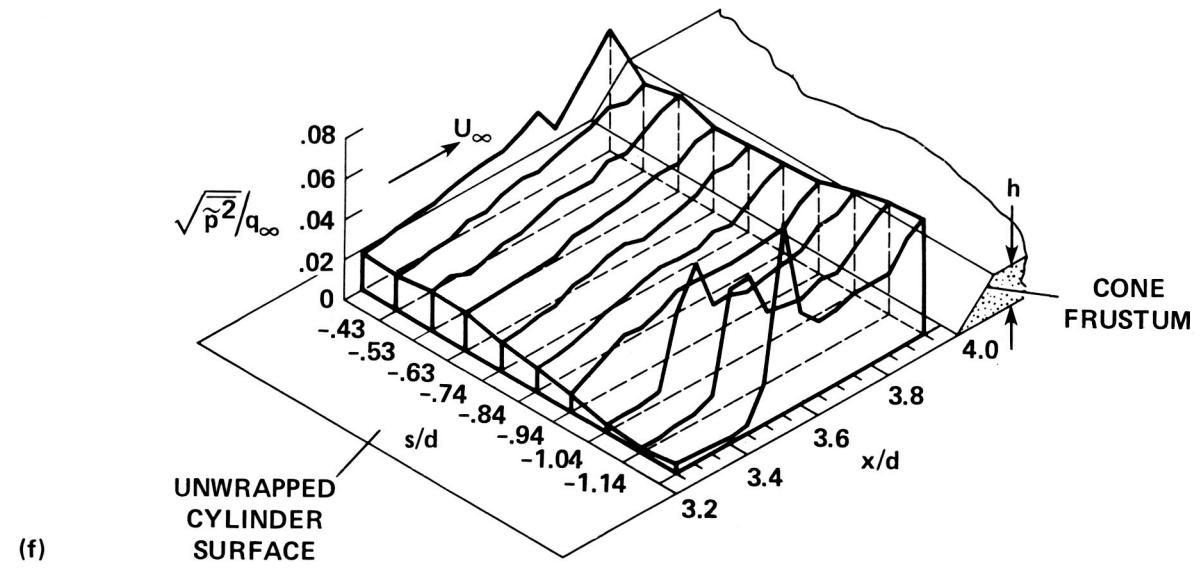

(f)

(e) Steady pressures; $\alpha = 8°$; $Re_d = 3.92 \times 10^6$.

(f) Fluctuating pressures; $\alpha = 8°$; $Re_d = 3.92 \times 10^6$.

Figure 8.– Continued.

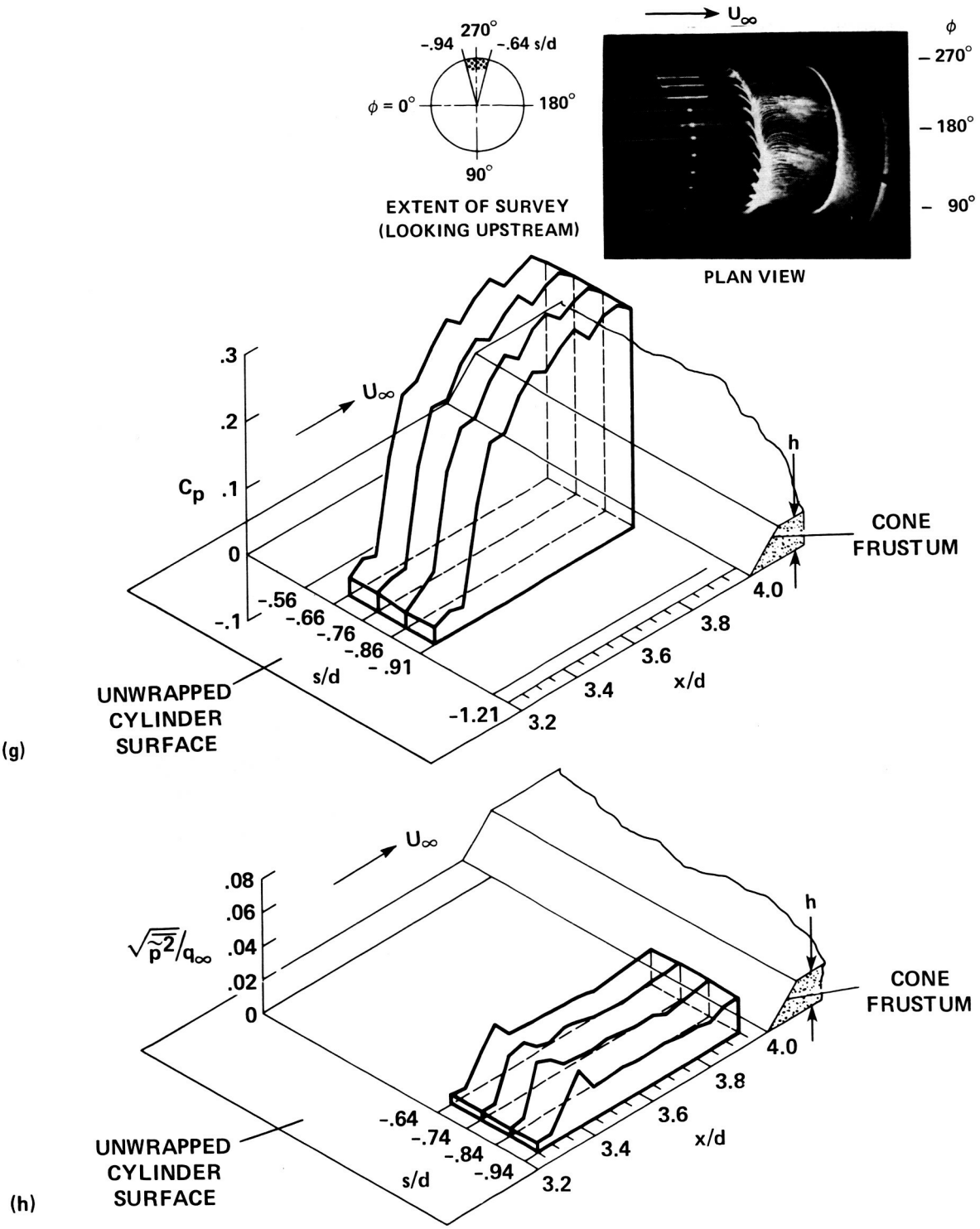

(g) Steady pressures; $\alpha = 0°$; $Re_d = 1.54 \times 10^6$.

(h) Fluctuating pressures; $\alpha = 0°$; $Re_d = 1.54 \times 10^6$.

Figure 8.– Continued.

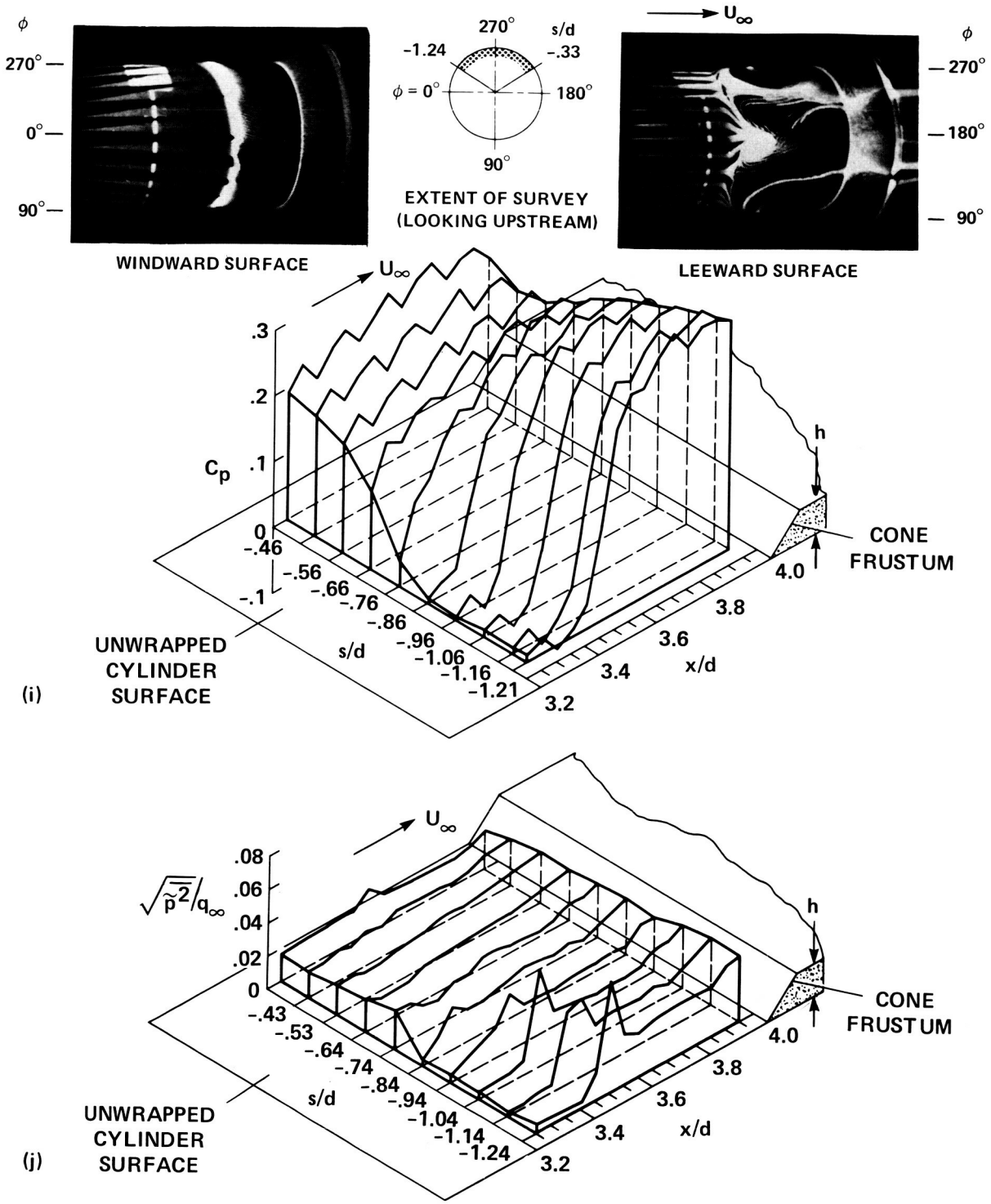

(i) Steady pressures; $\alpha = 4°$; $Re_d = 1.52 \times 10^6$.

(j) Fluctuating pressures; $\alpha = 4°$; $Re_d = 1.52 \times 10^6$.

Figure 8.– Continued.

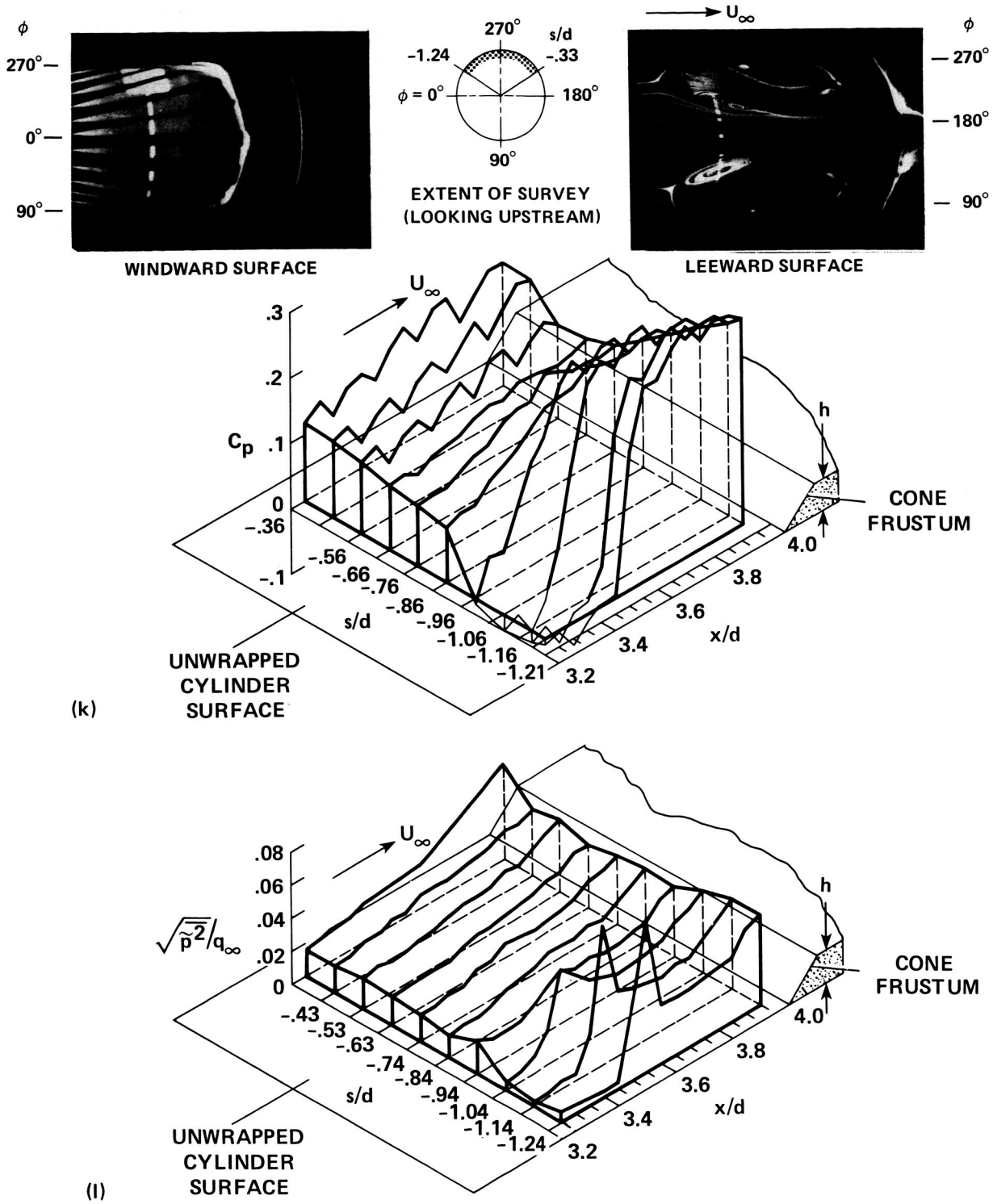

(k) Steady pressures; $\alpha = 8°$; $Re_d = 1.52 \times 10^6$.

(l) Fluctuating pressures; $\alpha = 8°$; $Re_d = 1.52 \times 10^6$.

Figure 8.– Concluded.

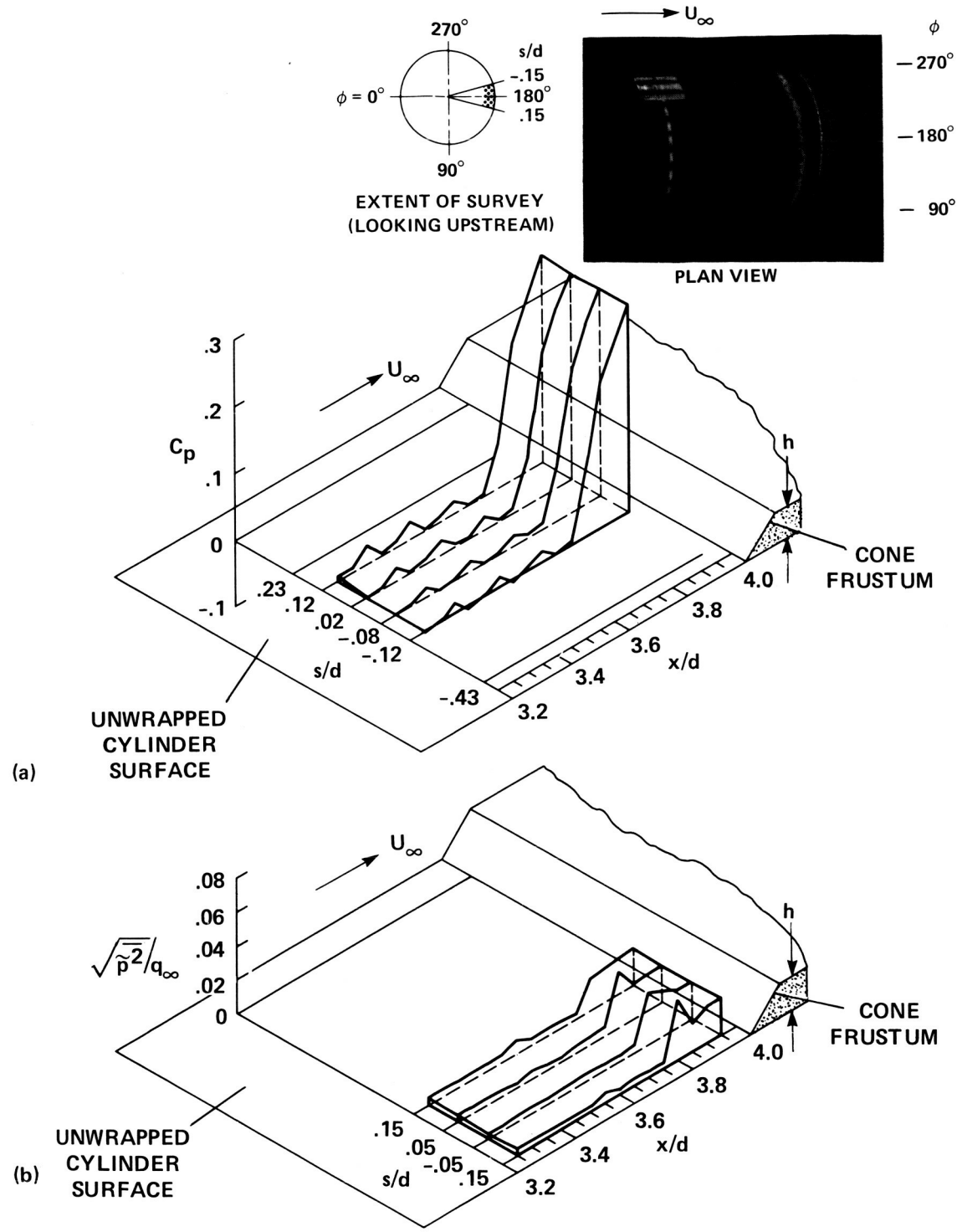

(a) Steady pressures; $\alpha = 0°$; $Re_d = 3.98 \times 10^6$.

(b) Fluctuating pressures; $\alpha = 0°$; $Re_d = 3.98 \times 10^6$.

Figure 9.– Longitudinal and circumferential variation of the steady and fluctuating pressures in the attached, shock, separated, and vortex flow regions ahead of a $\theta = 23°$ cone frustum and axisymmetric ring on the ogive-cylinder model at $M_\infty = 2.0$; $\beta = 0.2°$; $h = 0.0762$ m.

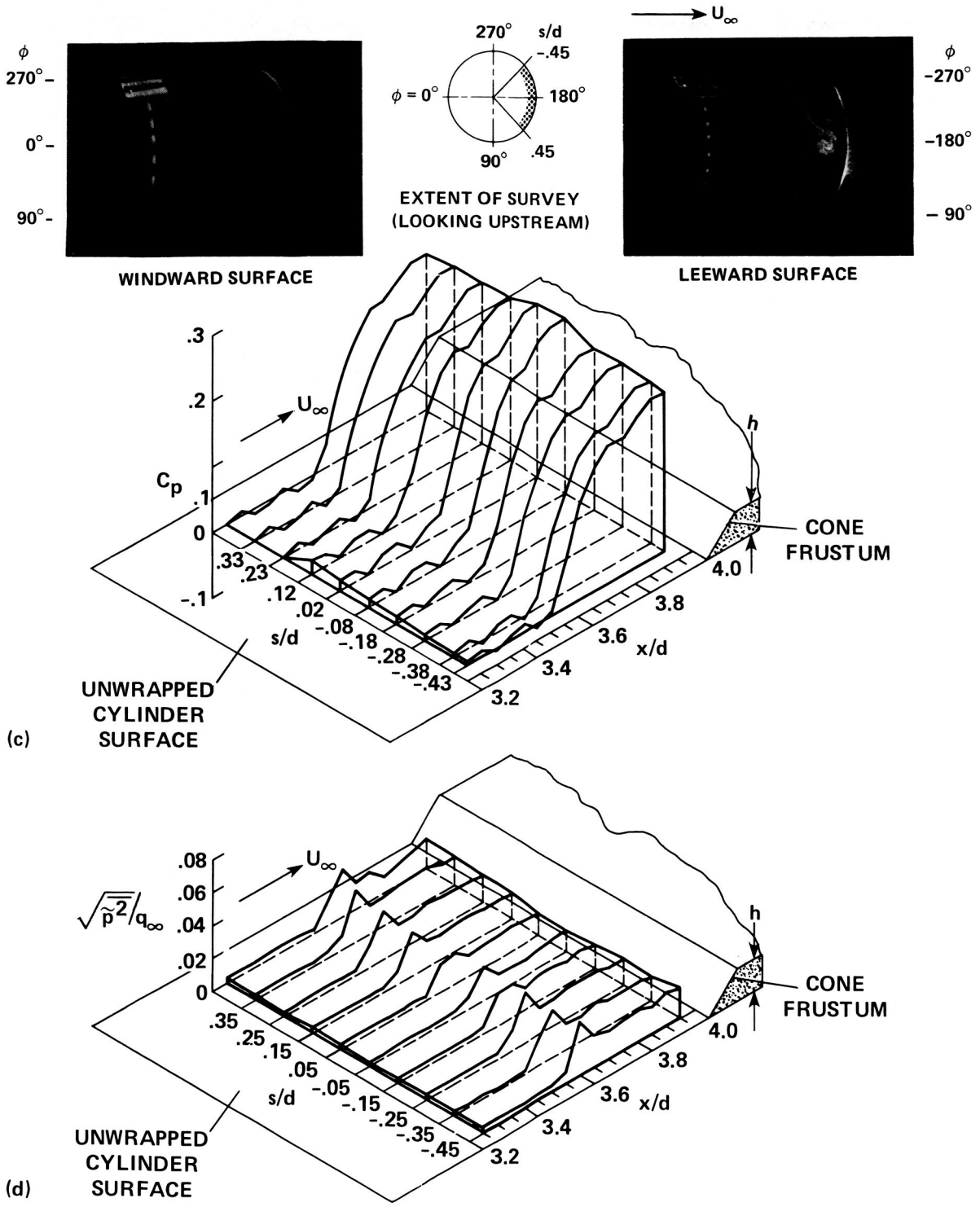

(c) Steady pressures; $\alpha = 4°$; $Re_d = 3.86 \times 10^6$.

(d) Fluctuating pressures; $\alpha = 4°$; $Re_d = 3.86 \times 10^6$.

Figure 9.– Continued.

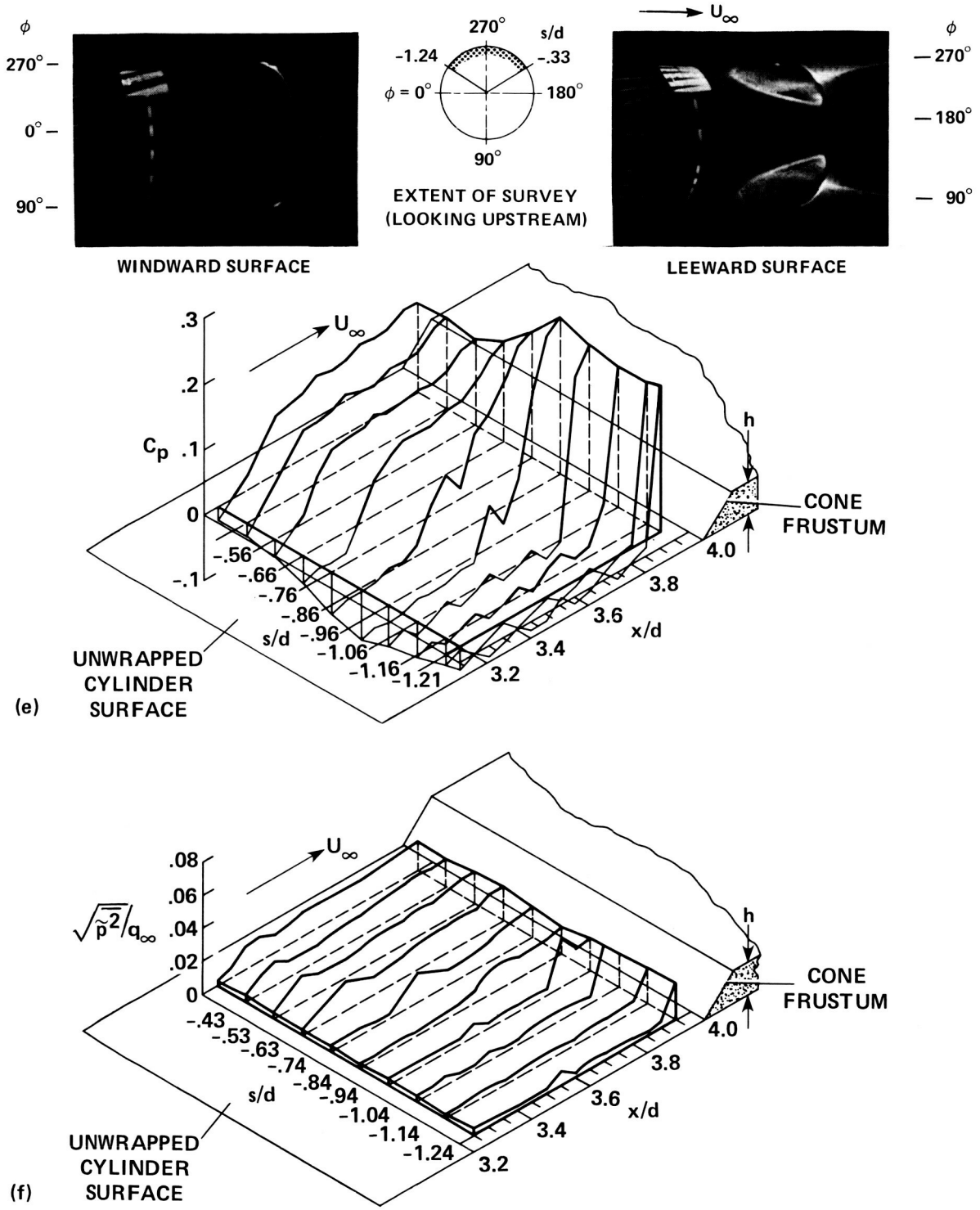

(e) Steady pressures; $\alpha = 8°$; $Re_d = 4.06 \times 10^6$.

(f) Fluctuating pressures; $\alpha = 8°$; $Re_d = 4.06 \times 10^6$.

Figure 9.– Continued.

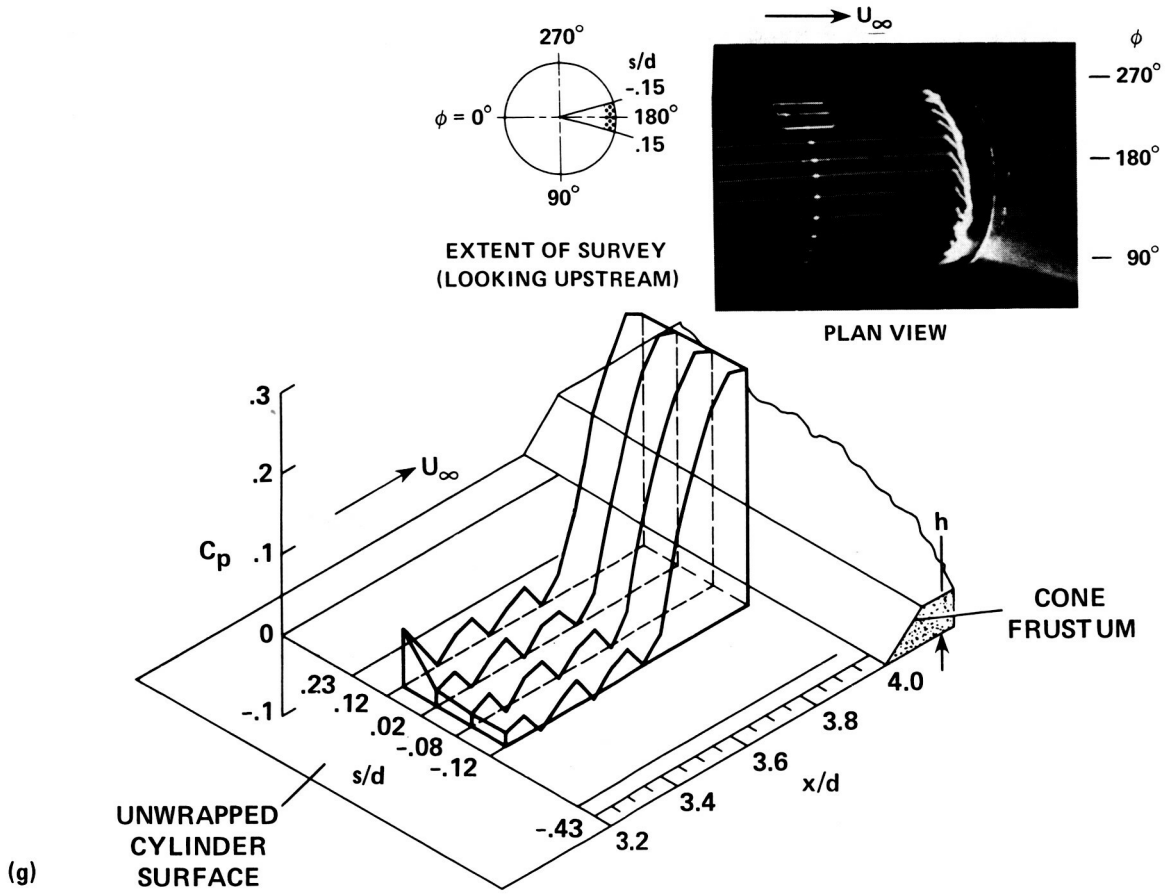

(g) Steady pressures; $\alpha = 0°$; $Re_d = 1.51 \times 10^6$.

(h) Fluctuating pressures; $\alpha = 0°$; $Re_d = 1.51 \times 10^6$.

Figure 9.– Continued.

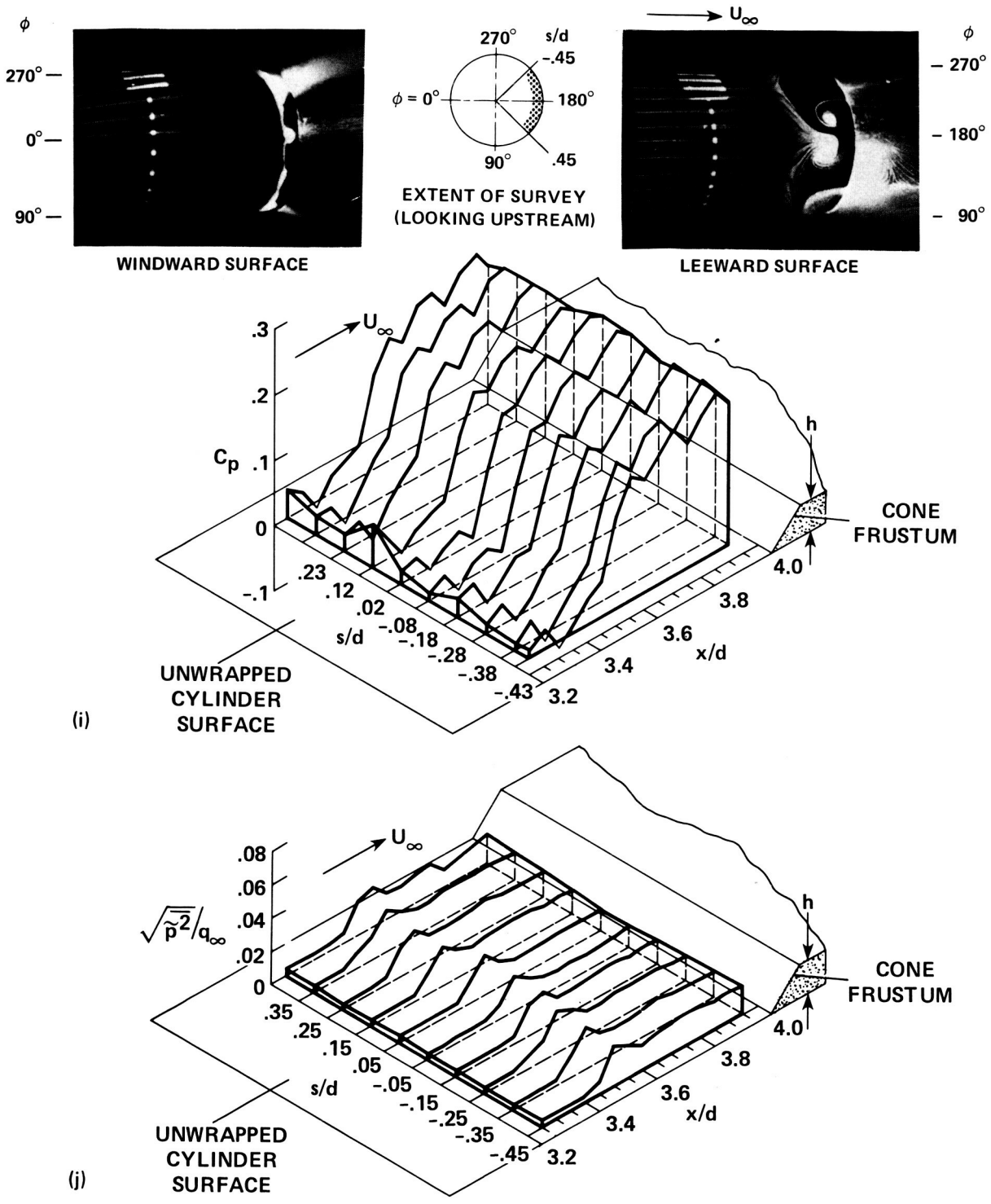

(i) Steady pressures; $\alpha = 4°$; $Re_d = 1.50 \times 10^6$.

(j) Fluctuating pressures; $\alpha = 4°$; $Re_d = 1.50 \times 10^6$.

Figure 9.– Continued.

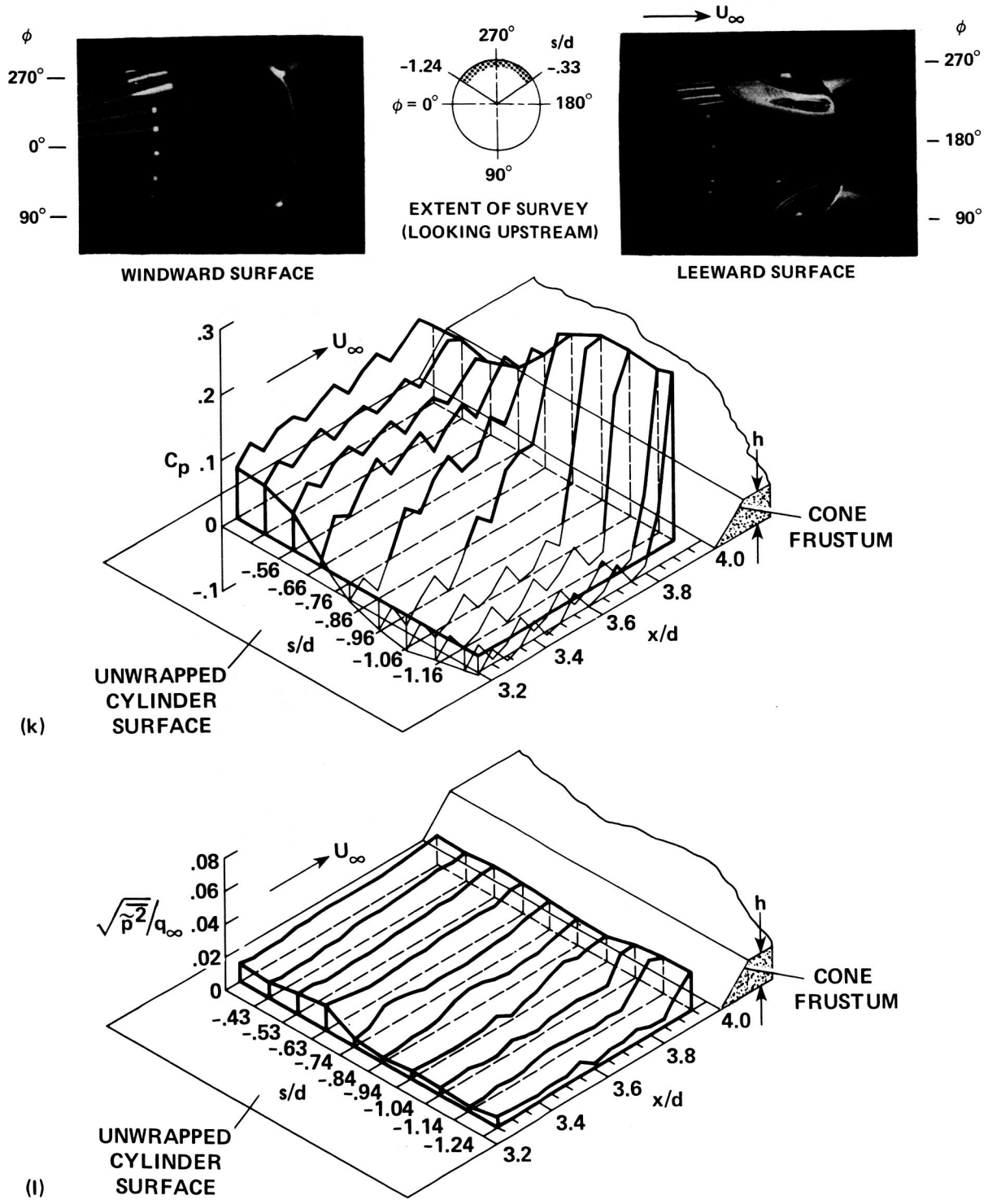

(k) Steady pressures; $\alpha = 8°$; $Re_d = 1.50 \times 10^6$.

(l) Fluctuating pressures; $\alpha = 8°$; $Re_d = 1.50 \times 10^6$.

Figure 9.– Concluded.

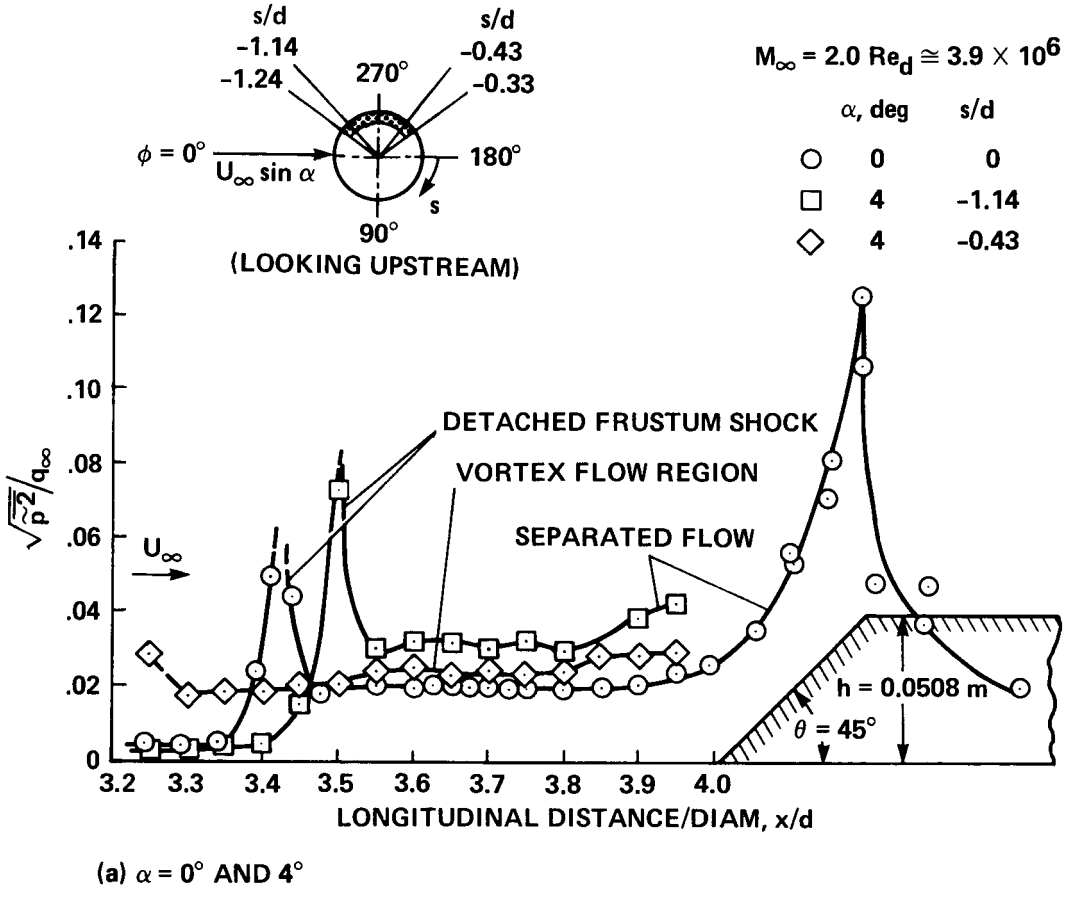

(a) $\alpha = 0°$ AND 4°

Figure 10.– Comparison of the fluctuating pressures in the vortex flow region with those of the detached frustum shock and the shock-separated flow region; $\theta = 45°$.

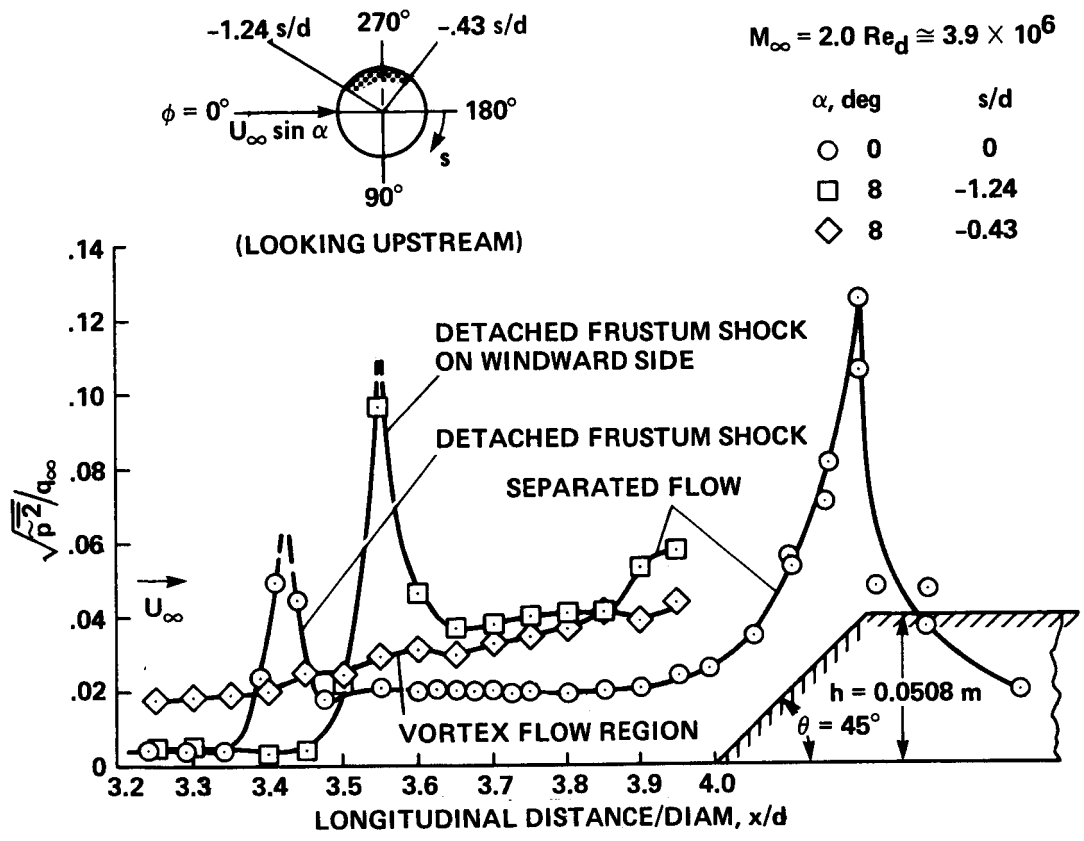

(b) α = 0° AND 8°

Figure 10.- Concluded.

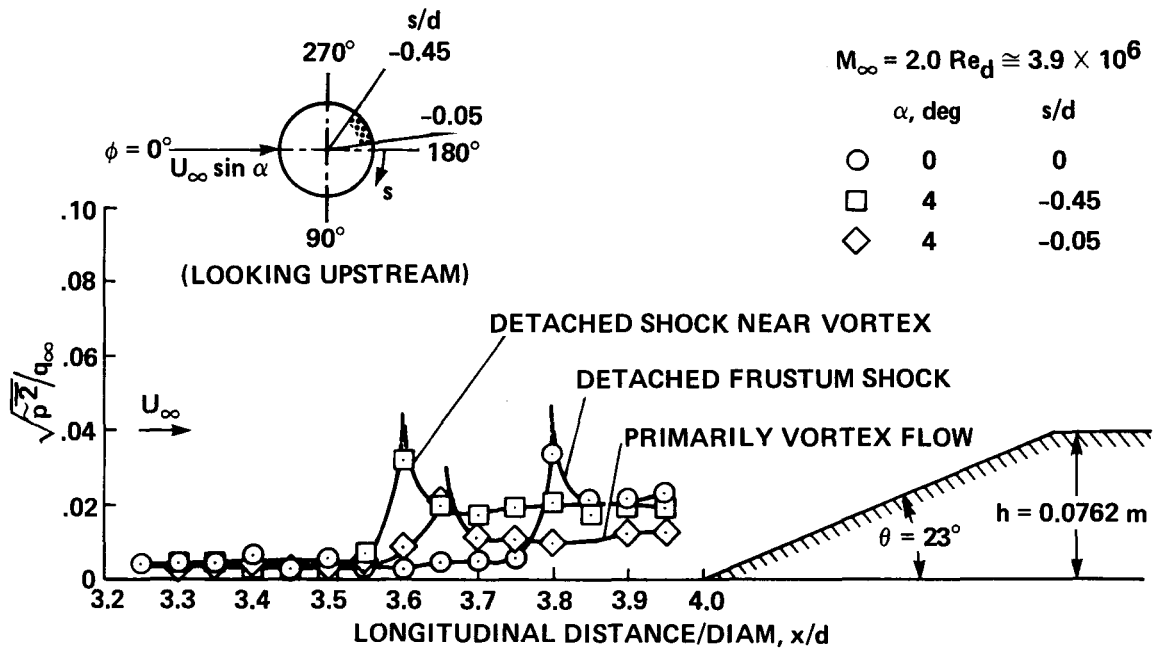

(a) $\alpha = 0°$ AND 4°

Figure 11.– Comparison of the fluctuating pressures in the vortex flow region with those of the detached frustum shock and the shock-separated flow region; $\theta = 23°$.

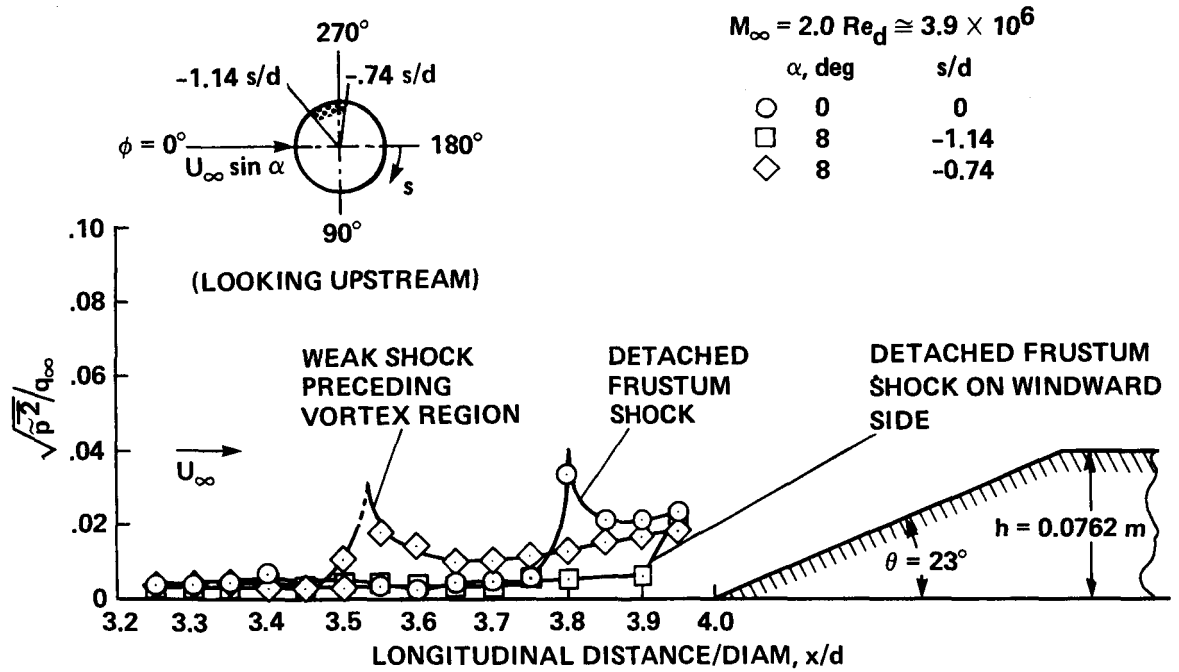

(b) $\alpha = 0°$ AND 8°

Figure 11.– Concluded.

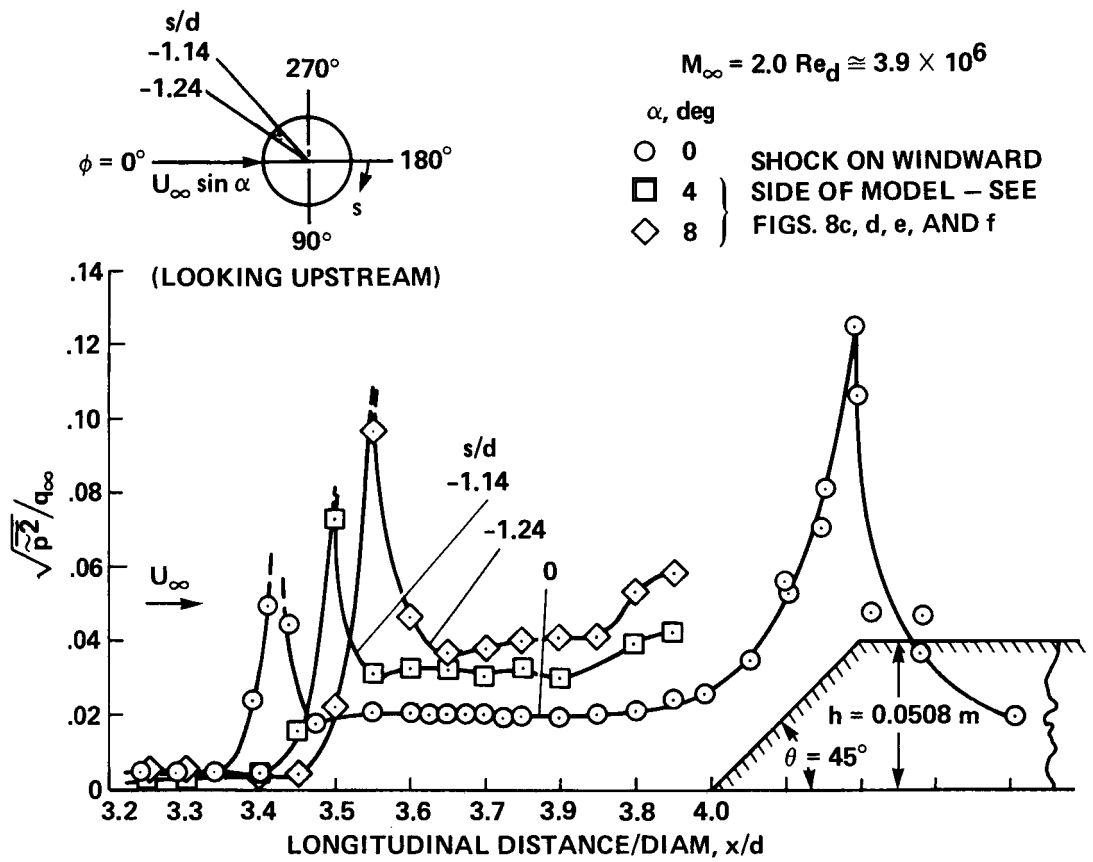

Figure 12.– Effect of angle of attack on the fluctuating pressures in the attached turbulent boundary layer, in the detached frustum shock, and in the shock-separated flow region for $\theta = 45°$.

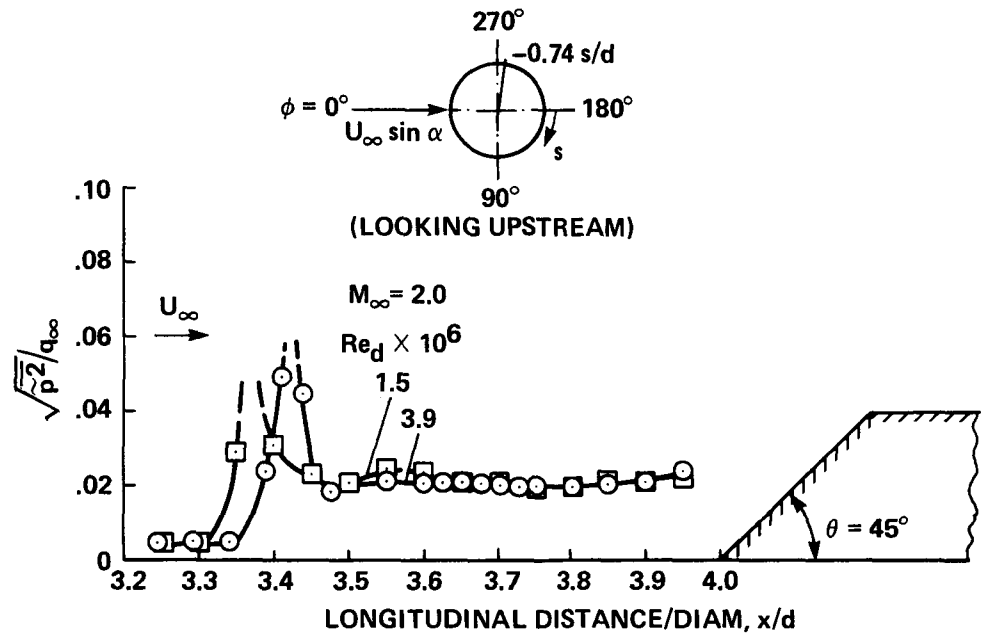

(a) $\alpha = 0°$; s/d = -0.74

Figure 13.– Effect of Reynolds number on the fluctuating pressures in the detached frustum shock and in the separated flow region; $\theta = 45°$; $h = 0.0508$ m.

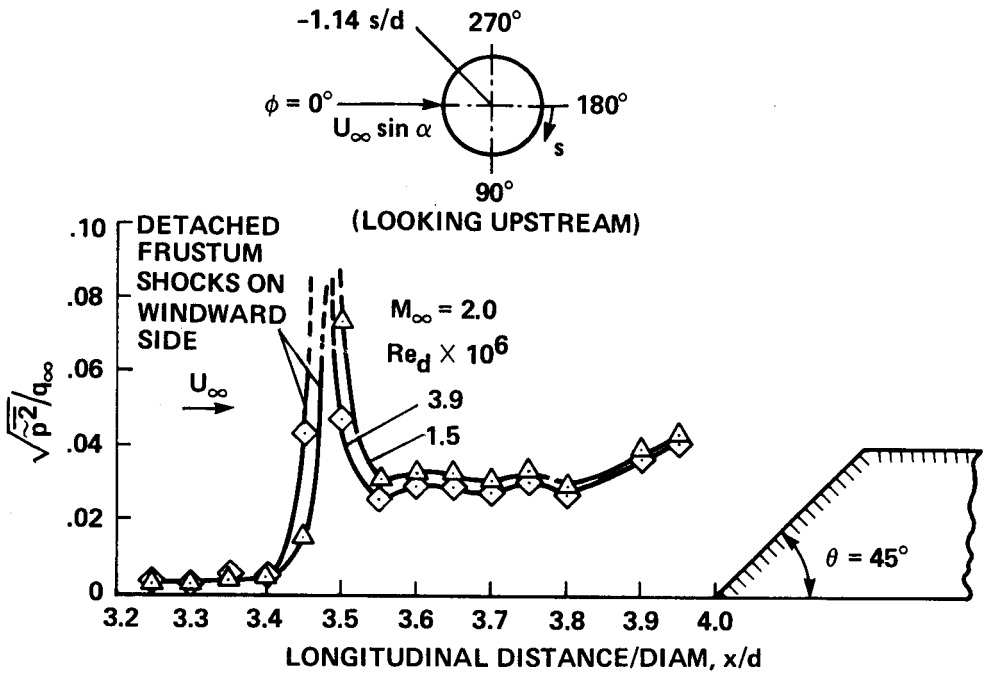

(b) $\alpha = 4°$; s/d = -1.14

Figure 13.– Continued.

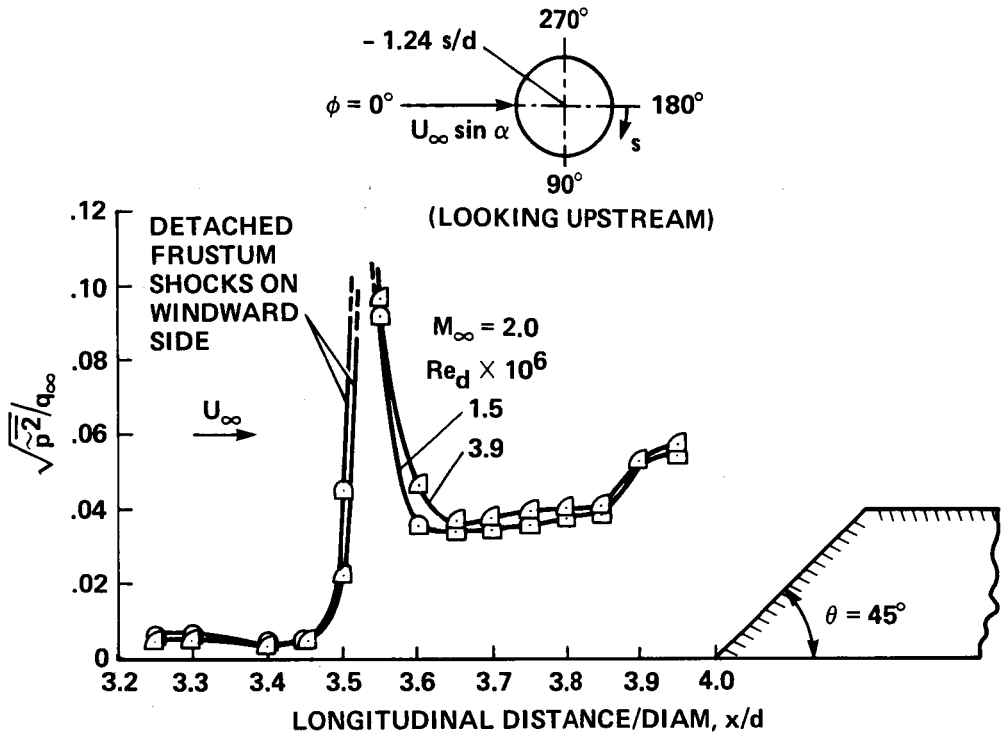

(c) $\alpha = 8°$; s/d = -1.24

Figure 13.– Concluded.

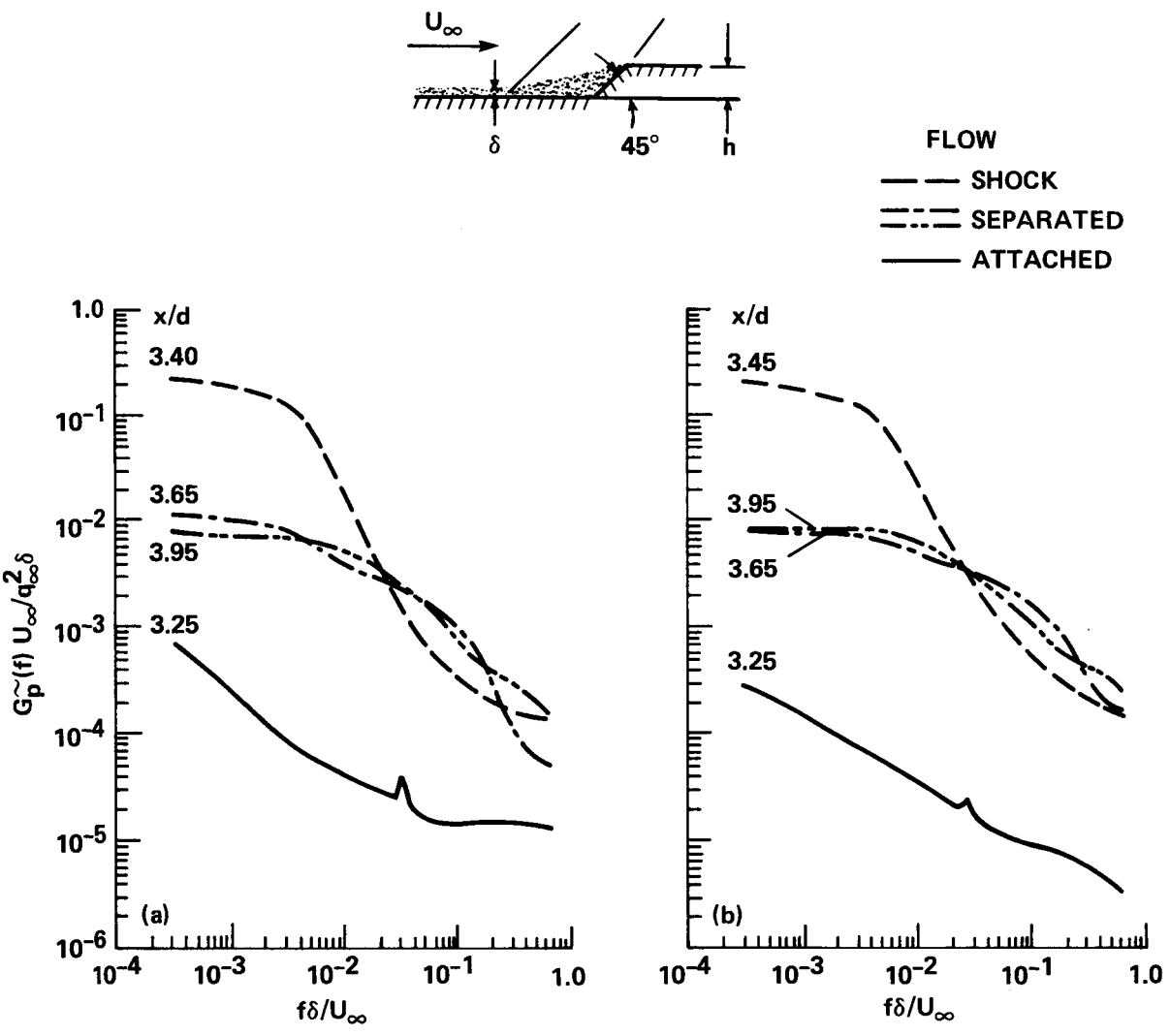

(a) $Re_d = 1.54 \times 10^6$; $s/d = -0.64$.

(b) $Re_d = 3.94 \times 10^6$; $s/d = -0.84$.

Figure 14.– Power spectra of the pressure fluctuations for various types of flow ahead of the $\theta = 45°$ cone frustum with no crossflow ($\alpha = 0°$); $M_\infty = 2.0$.

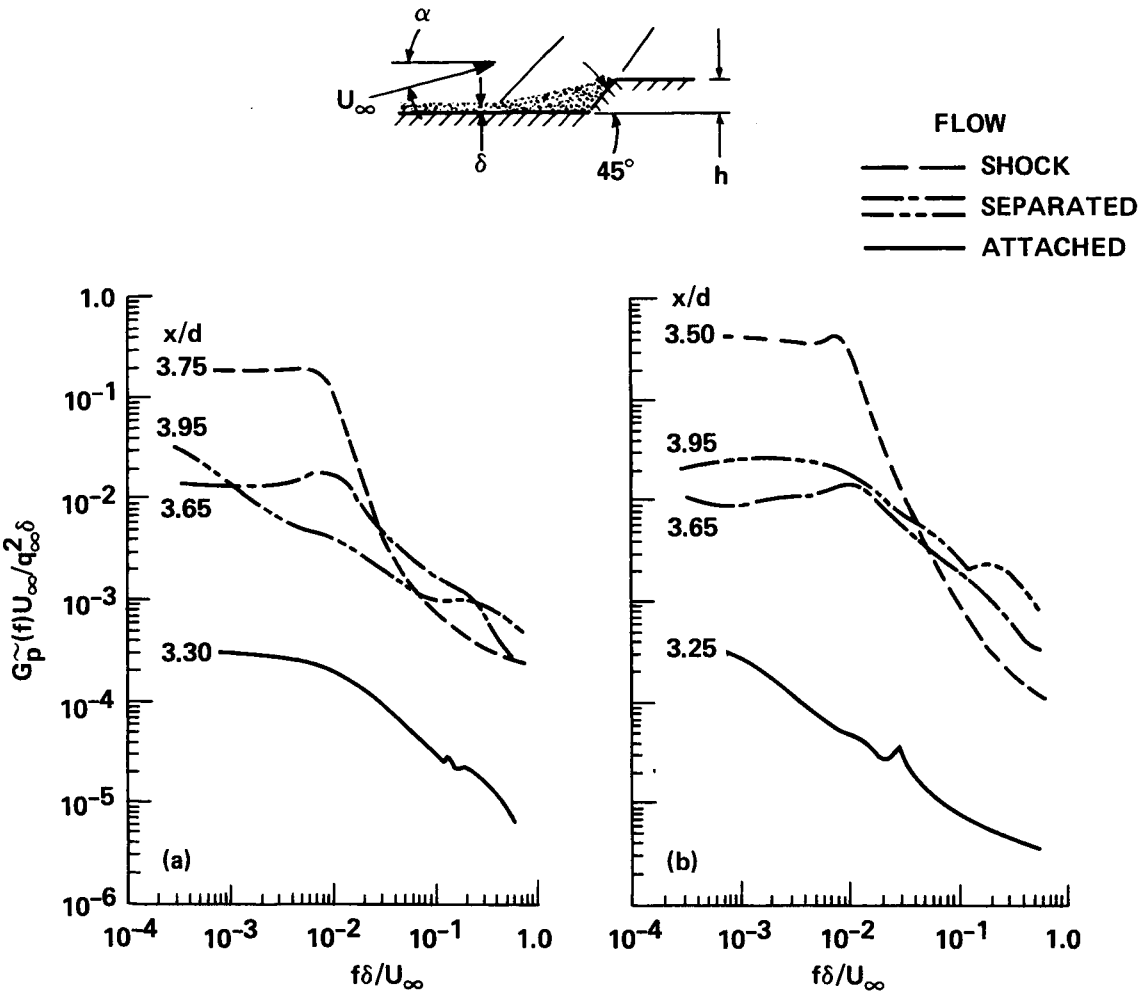

(a) $Re_d = 1.52\times10^6$; $s/d = -1.24$.

(b) $Re_d = 3.88\times10^6$; $s/d = -1.14$.

Figure 15.– Power spectra of the pressure fluctuations for various types of flow ahead of the $\theta = 45°$ cone frustum with small crossflow ($\alpha = 4°$); $M_\infty = 2.0$.

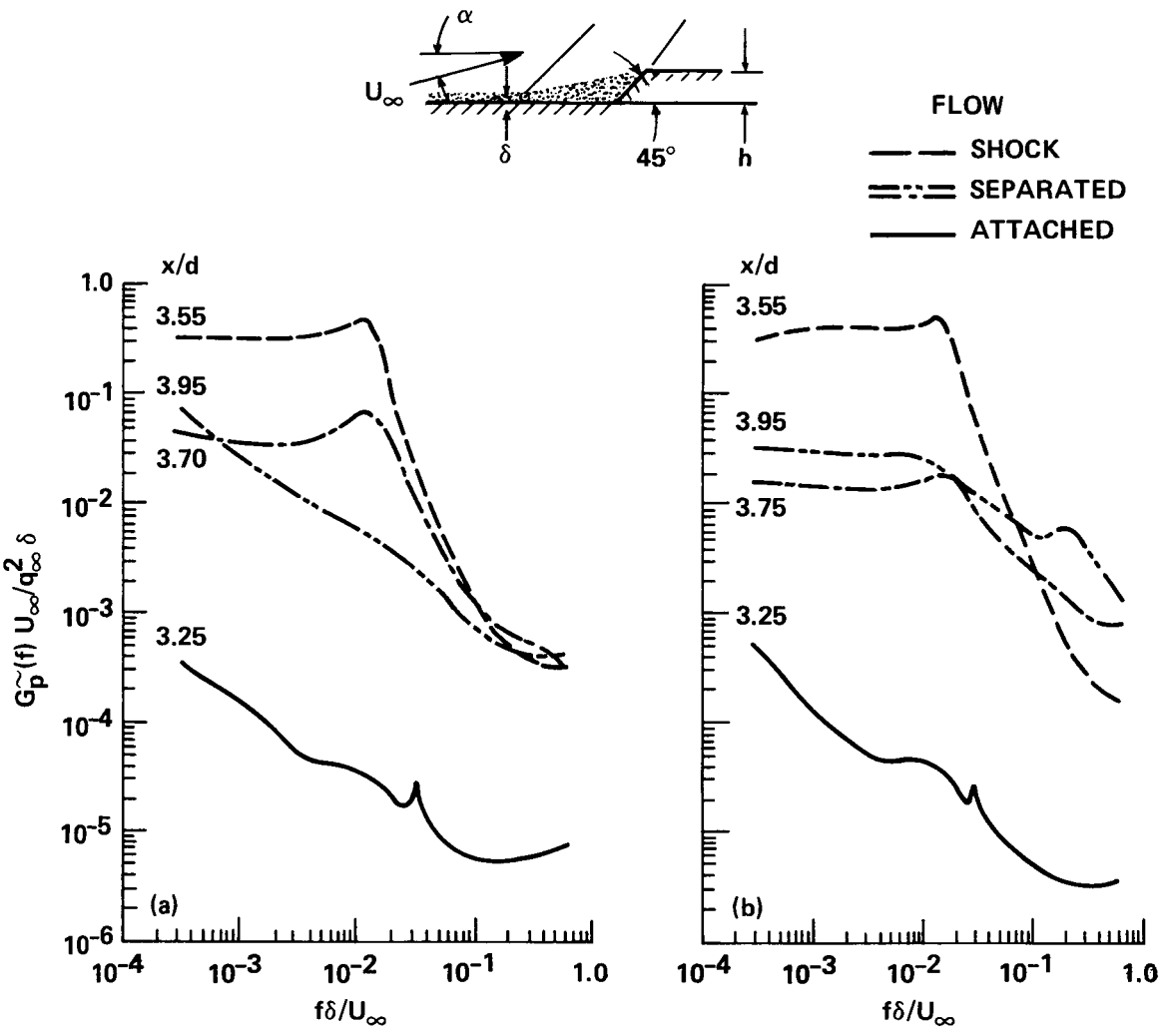

(a) $Re_d = 1.52 \times 10^6$.

(b) $Re_d = 3.92 \times 10^6$.

Figure 16.– Power spectra of the pressure fluctuations for various types of flow ahead of the $\theta = 45°$ cone frustum with large crossflow ($\alpha = 8°$); $M_\infty = 2.0$; $s/d = -1.24$.

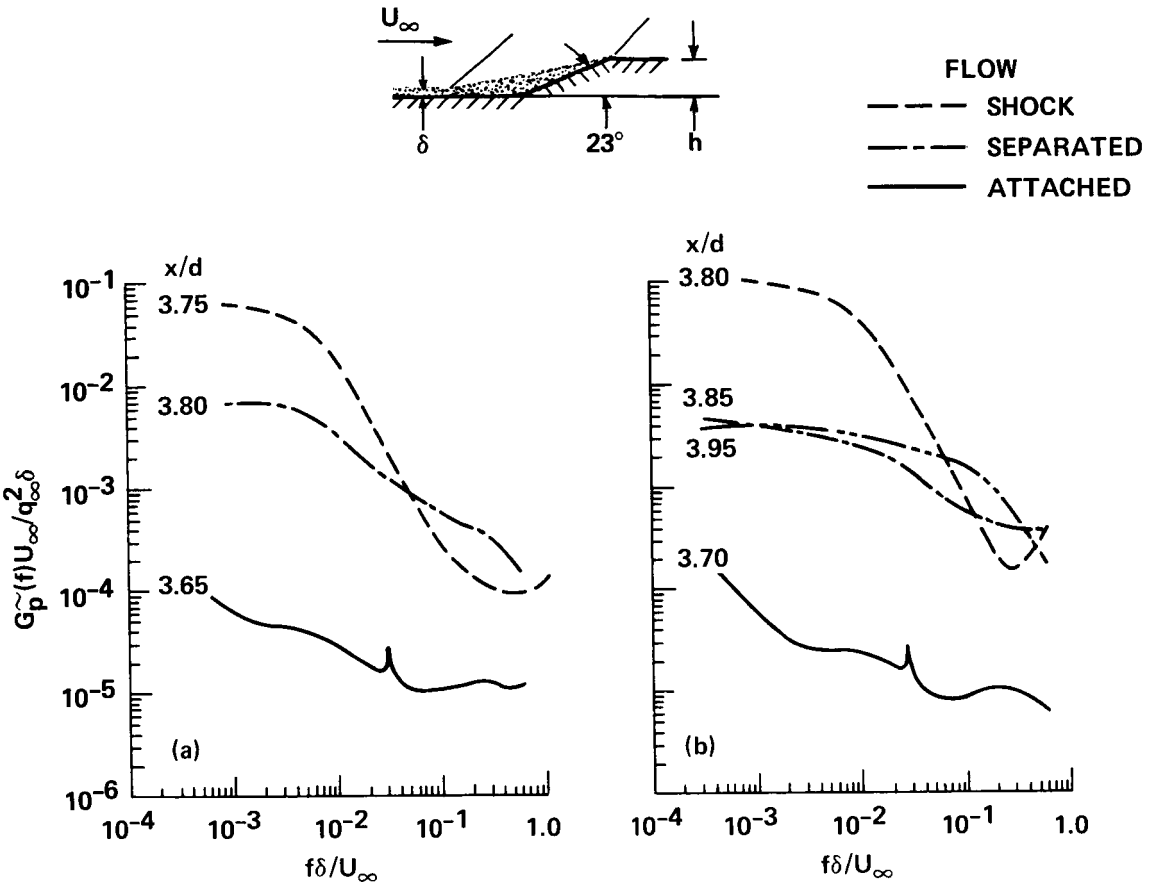

(a) $Re_d = 1.51\times10^6$.

(b) $Re_d = 3.98\times10^6$.

Figure 17.– Power spectra of the pressure fluctuations for various types of flow ahead of the $\theta = 23°$ cone frustum with no crossflow ($\alpha = 0°$); $M_\infty = 2.0$; $s/d = -0.15$.

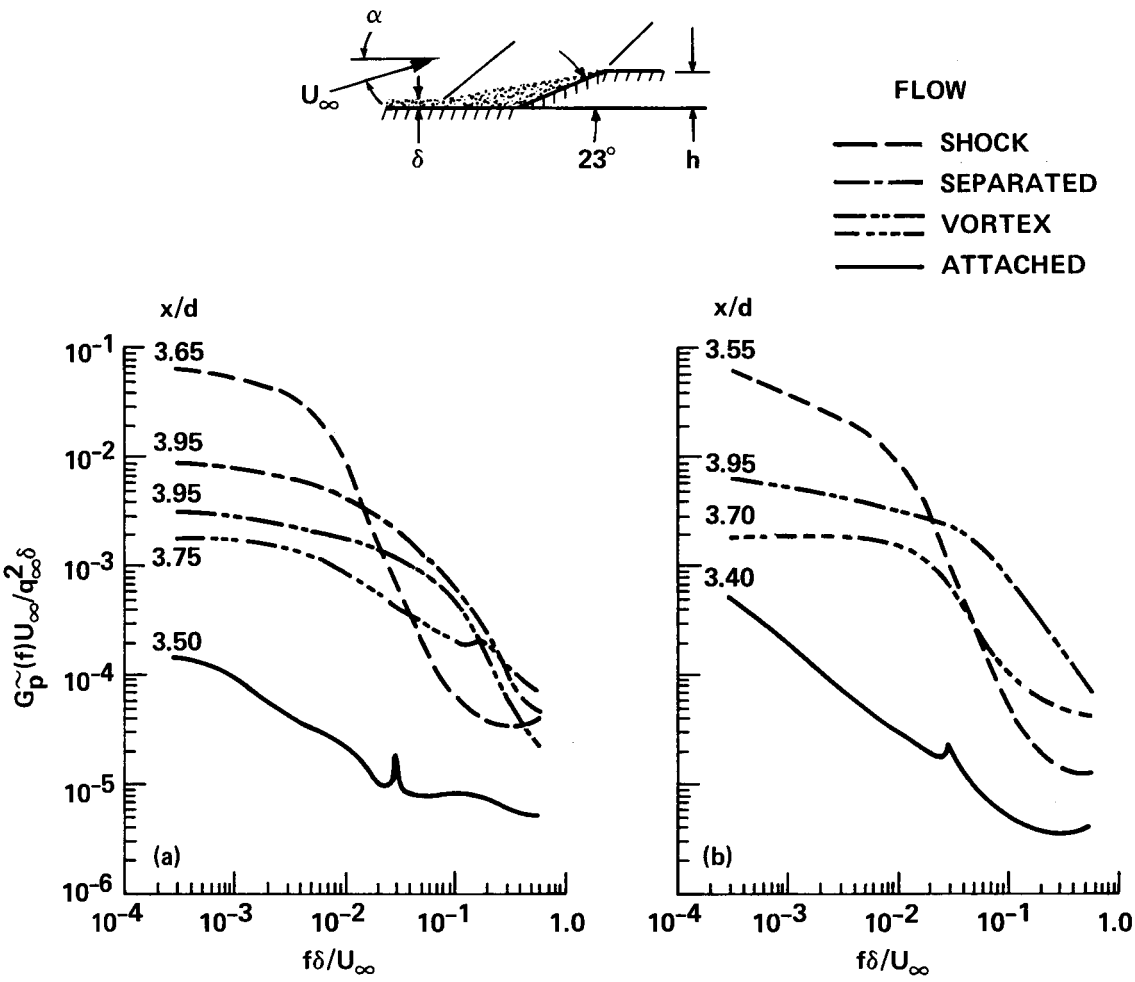

(a) Small crossflow ($\alpha = 4°$); $s/d = -0.05$.

(b) Large crossflow ($\alpha = 8°$); $s/d = -0.74$.

Figure 18.– Power spectra of the pressure fluctuations for various types of flow ahead of the $\theta = 23°$ cone frustum with small and large crossflows; $M_\infty = 2.0$; $Re_d \cong 3.9 \times 10^6$.

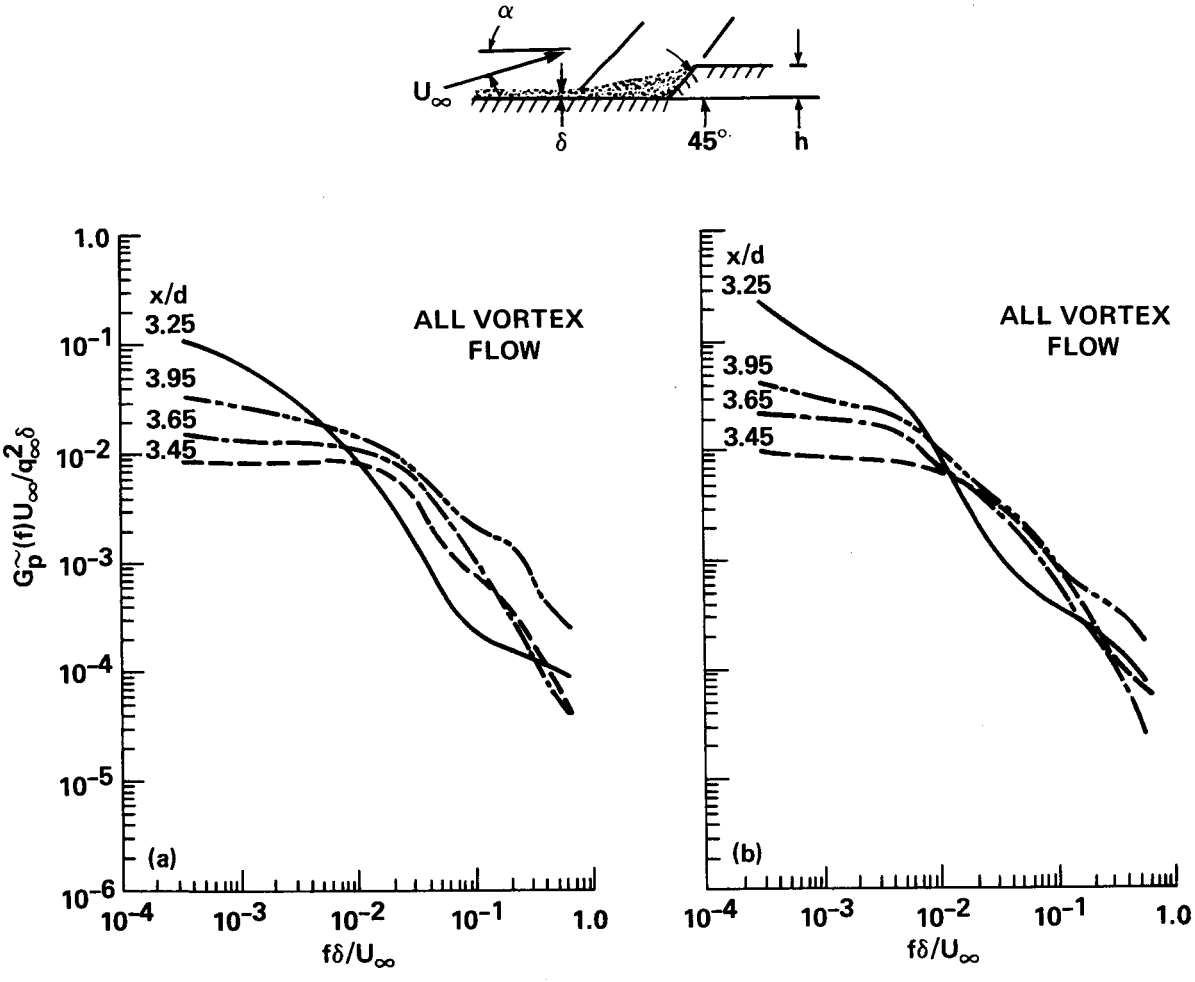

(a) $Re_d = 1.52 \times 10^6$; $s/d = -0.64$.

(b) $Re_d = 3.88 \times 10^6$; $s/d = -0.33$.

Figure 19.– Effect of longitudinal distance on the power spectra of the pressure fluctuations in the vortex flow region ahead of the $\theta = 45°$ cone frustum with small crossflow ($\alpha = 4°$); $M_\infty = 2.0$.

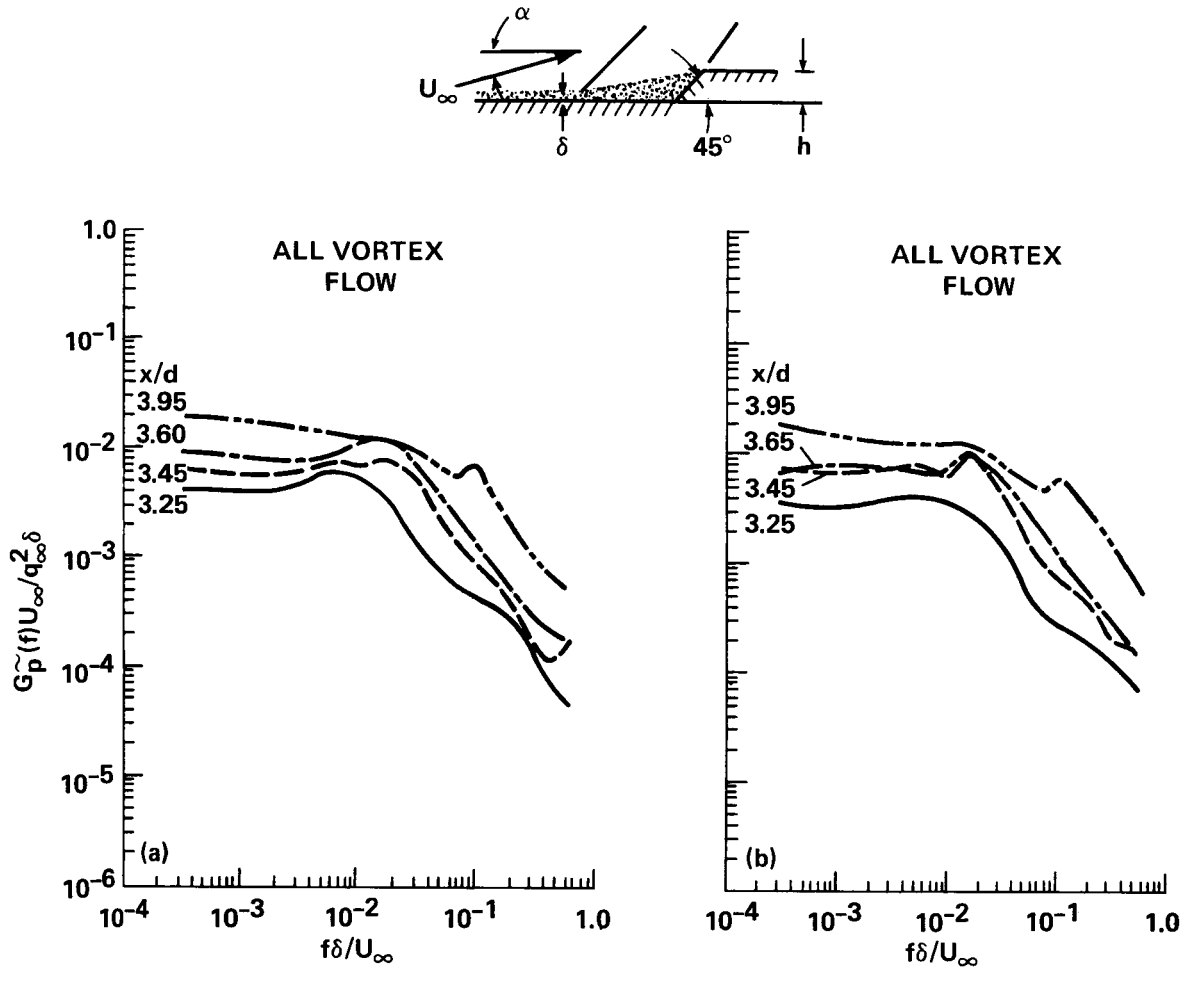

(a) $Re_d = 1.52 \times 10^6$.

(b) $Re_d = 3.92 \times 10^6$.

Figure 20.– Effect of longitudinal distance on the power spectra of the pressure fluctuations in the vortex flow region ahead of the $\theta = 45^\circ$ cone frustum with large crossflow ($\alpha = 8^\circ$); $M_\infty = 2.0$; $s/d = -0.74$.

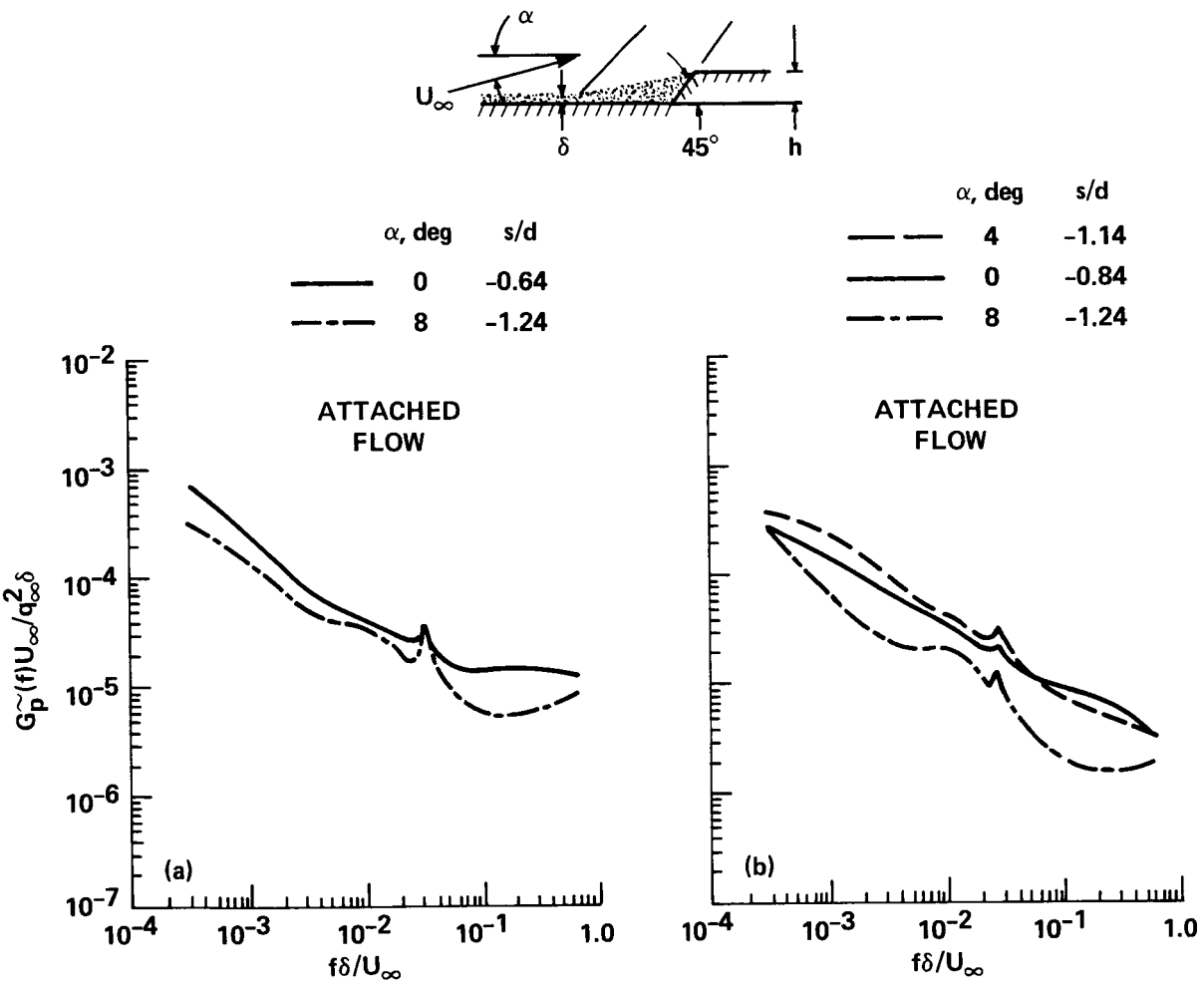

(a) $Re_d \cong 1.5\times10^6$.

(b) $Re_d \cong 3.9\times10^6$.

Figure 21.– Effect of angle of attack on the power spectra of the pressure fluctuations in the attached flow region ahead of the $\theta = 45°$ cone frustum; $M_\infty = 2.0$; $x/d = 3.25$.

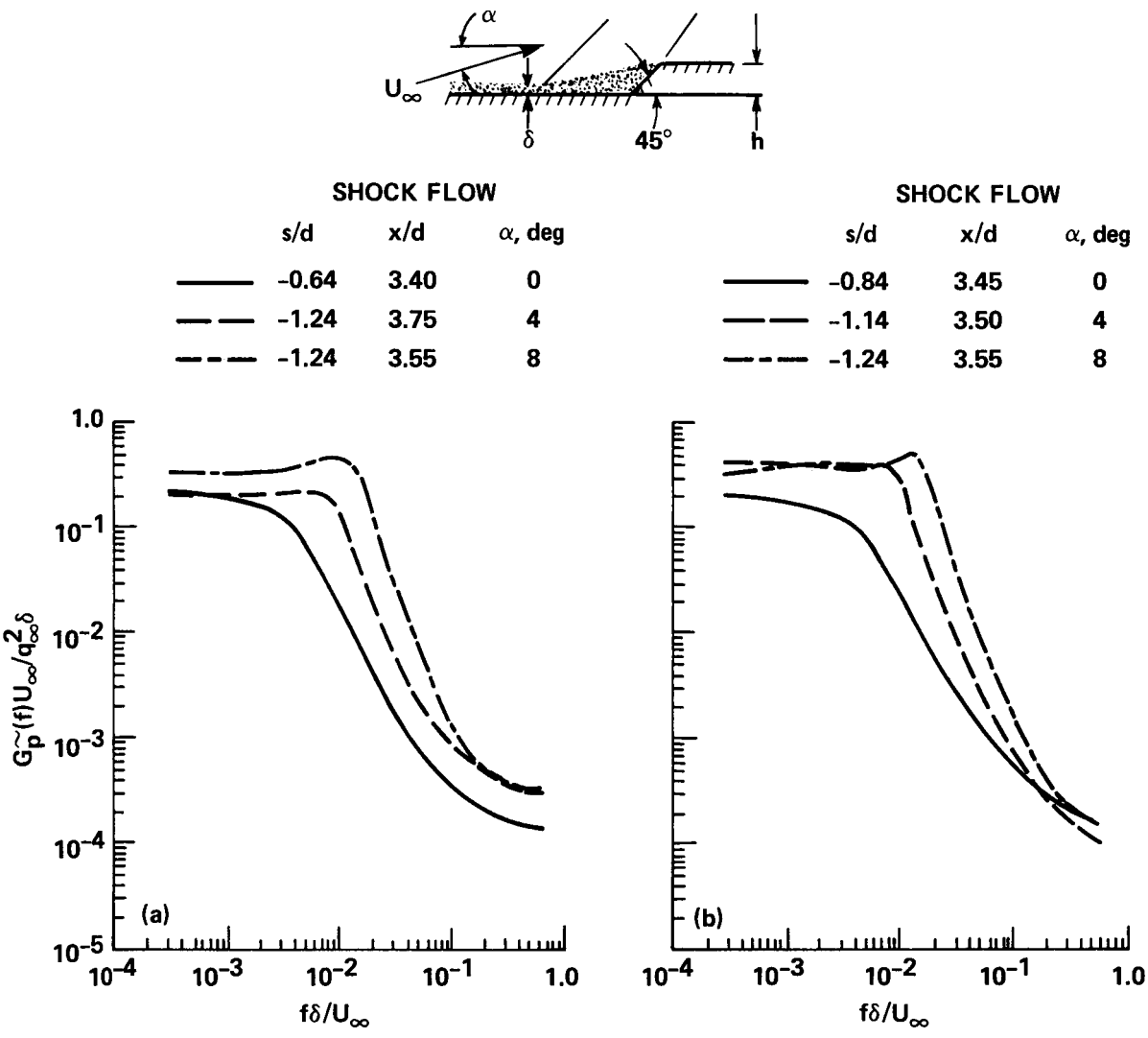

(a) $Re_d \cong 1.5\text{X}10^6$.

(b) $Re_d \cong 3.9\text{X}10^6$.

Figure 22.– Effect of angle of attack on the power spectra of the pressure fluctuations in the shock wave ahead of the $\theta = 45°$ cone frustum; $M_\infty = 2.0$.

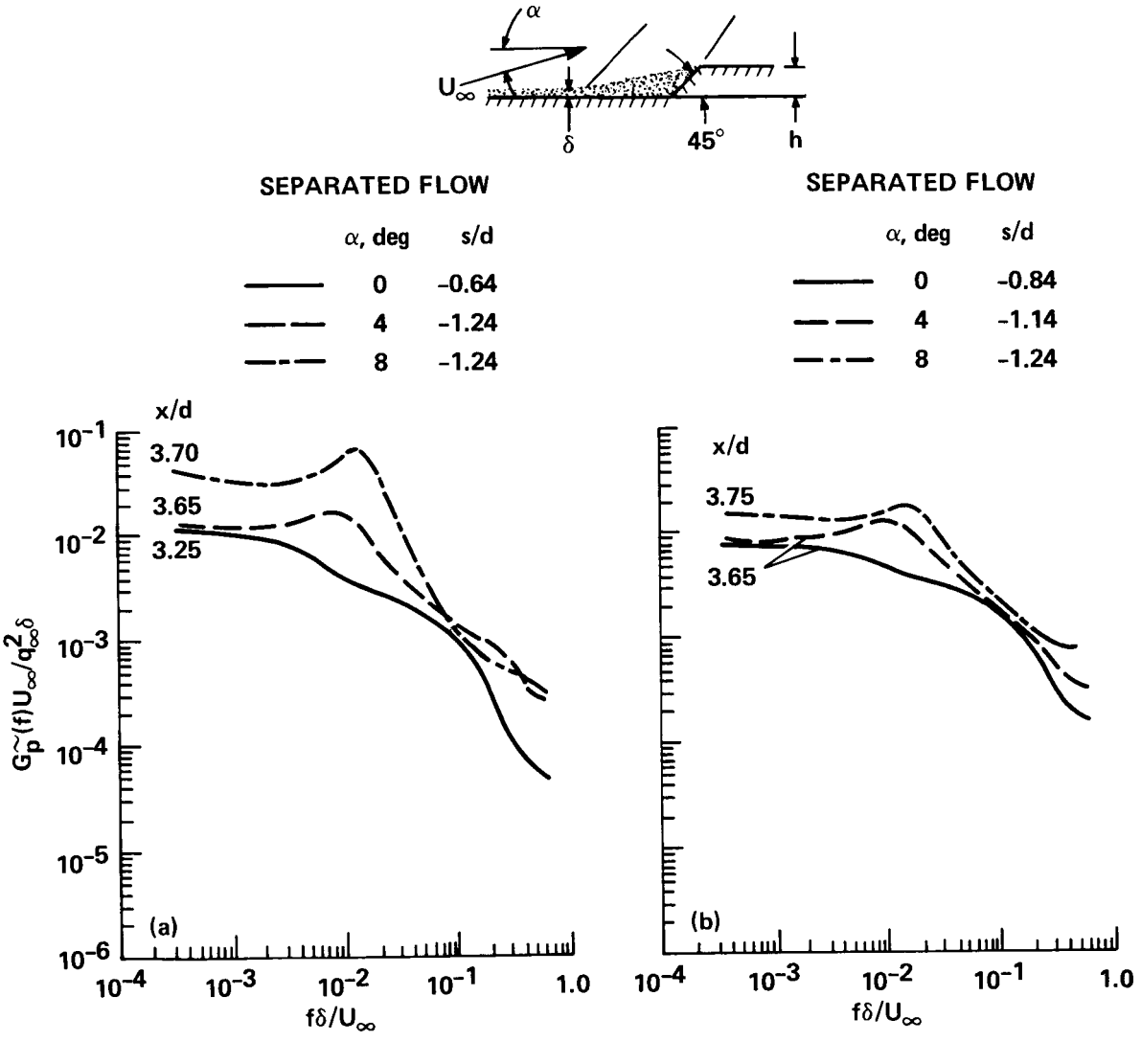

(a) $Re_d \cong 1.5 \times 10^6$.

(b) $Re_d \cong 3.9 \times 10^6$.

Figure 23.– Effect of angle of attack on the power spectra of the pressure fluctuations in the separated flow region ahead of the $\theta = 45°$ cone frustum; $M_\infty = 2.0$.

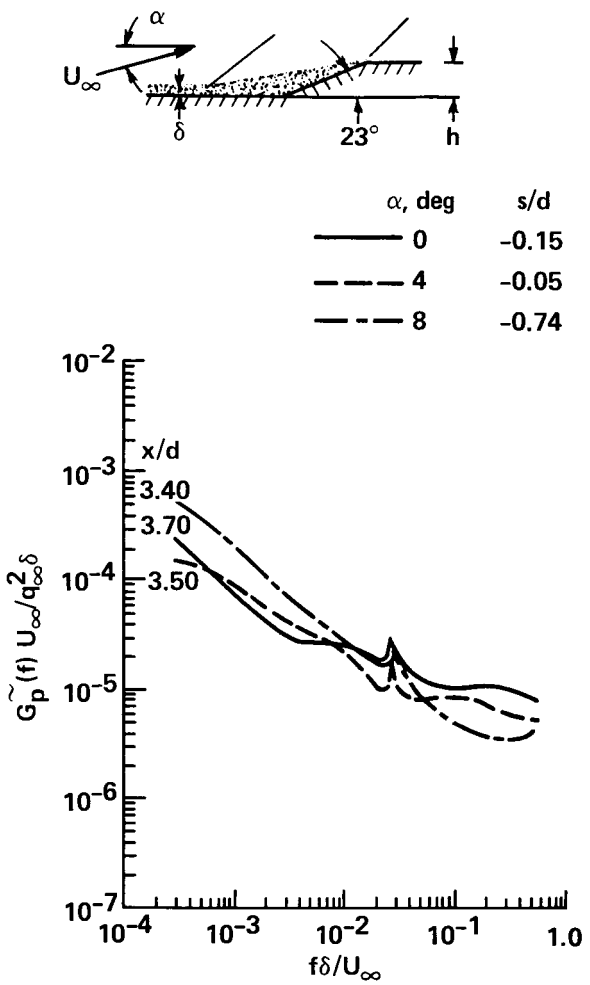

Figure 24.– Effect of angle of attack on the power spectra of the pressure fluctuations in the attached flow region ahead of the $\theta = 23^\circ$ cone frustum; $M_\infty = 2.0$; $Re_d \cong 3.9 \times 10^6$.

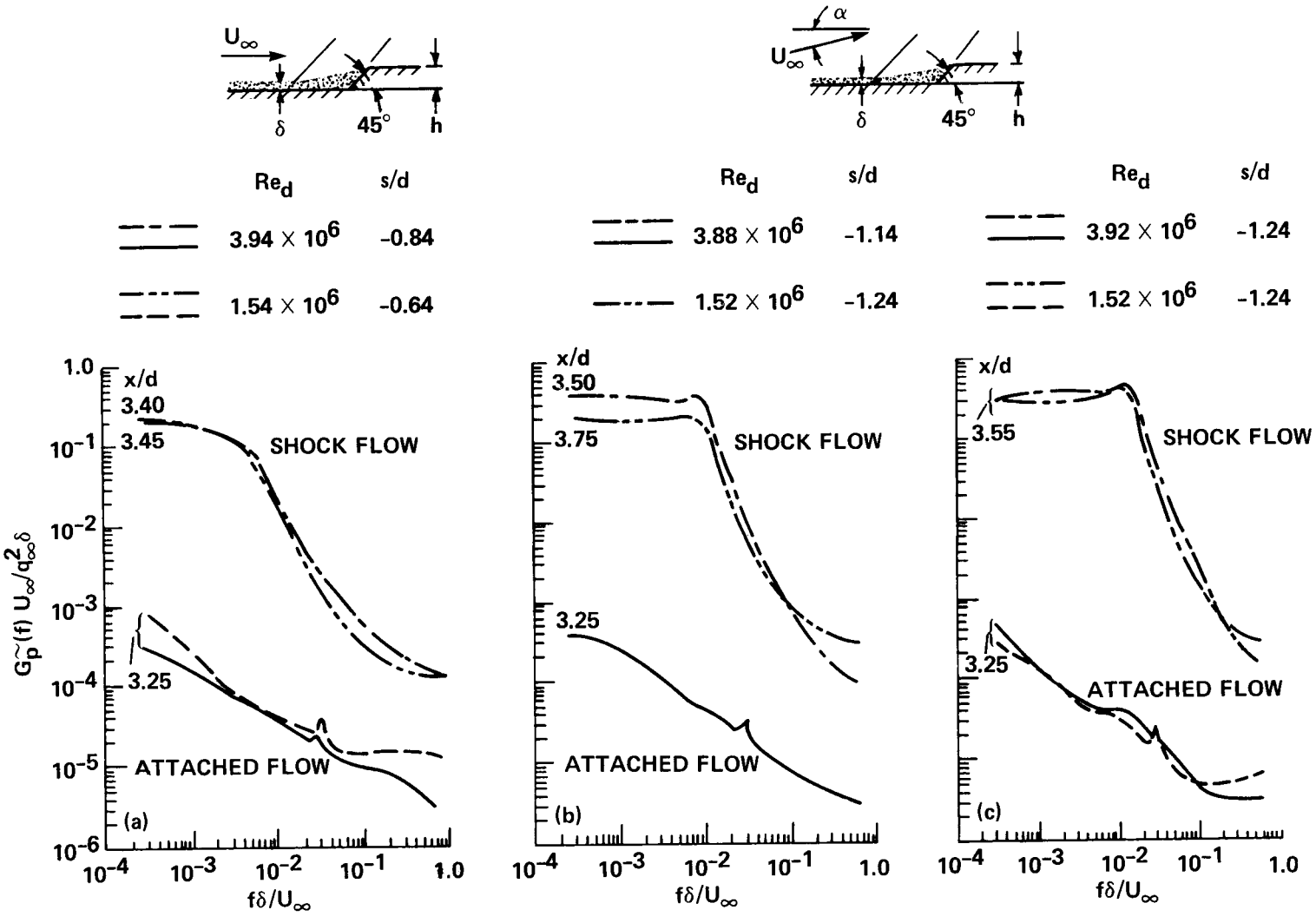

(a) No crossflow ($\alpha = 0°$).

(b) Small crossflow ($\alpha = 4°$).

(c) Large crossflow ($\alpha = 8°$).

Figure 25.– Effect of Reynolds number on the power spectra of the pressure fluctuations in the attached and shock flow regions ahead of the $\theta = 45°$ cone frustum for various crossflows; $M_\infty = 2.0$.

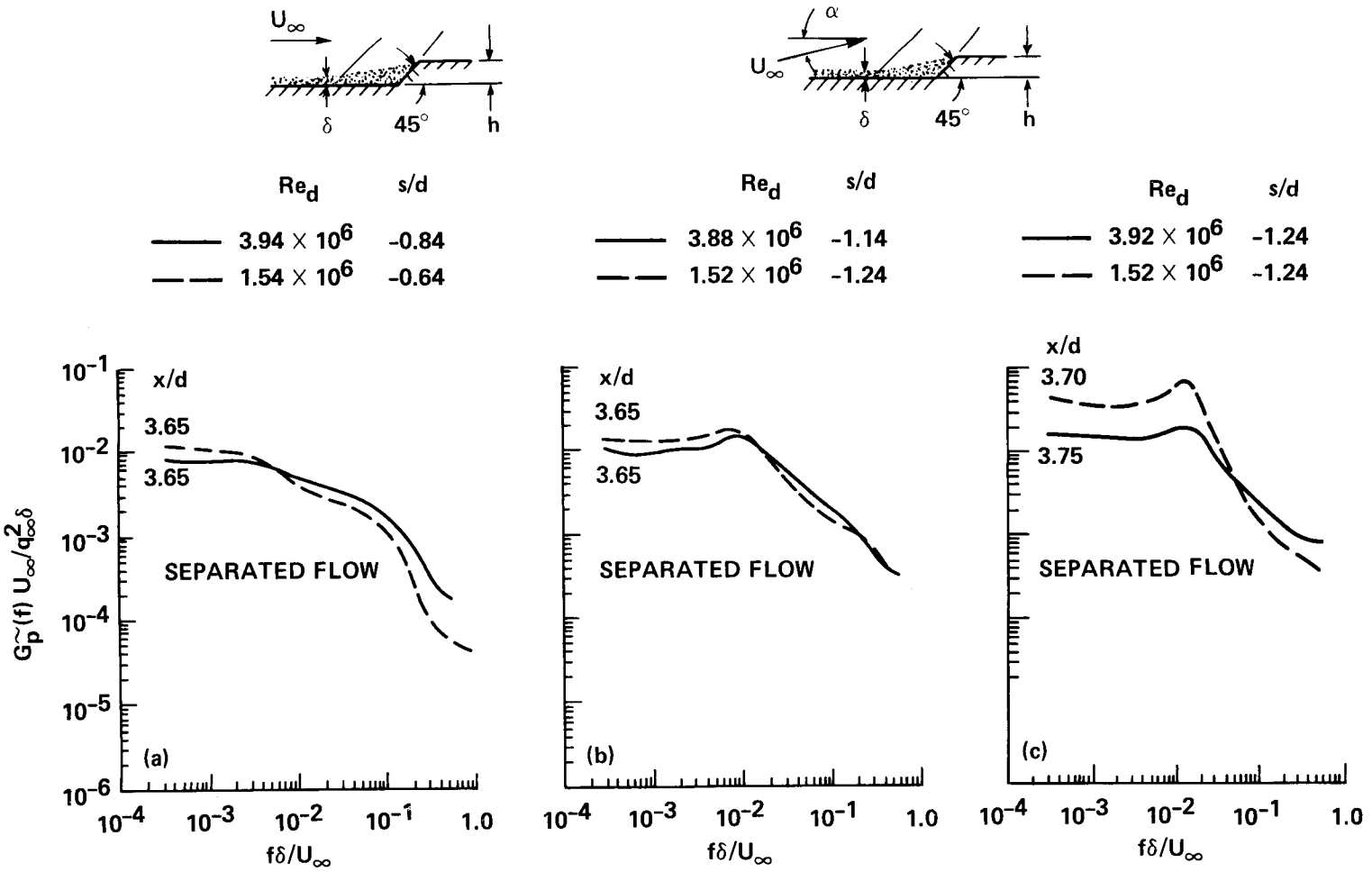

(a) No crossflow ($\alpha = 0°$).

(b) Small crossflow ($\alpha = 4°$).

(c) Large crossflow ($\alpha = 8°$).

Figure 26.– Effect of Reynolds number on the power spectra of the pressure fluctuations in the separated flow region ahead of the $\theta = 45°$ cone frustum for various crossflows; $M_\infty = 2.0$.

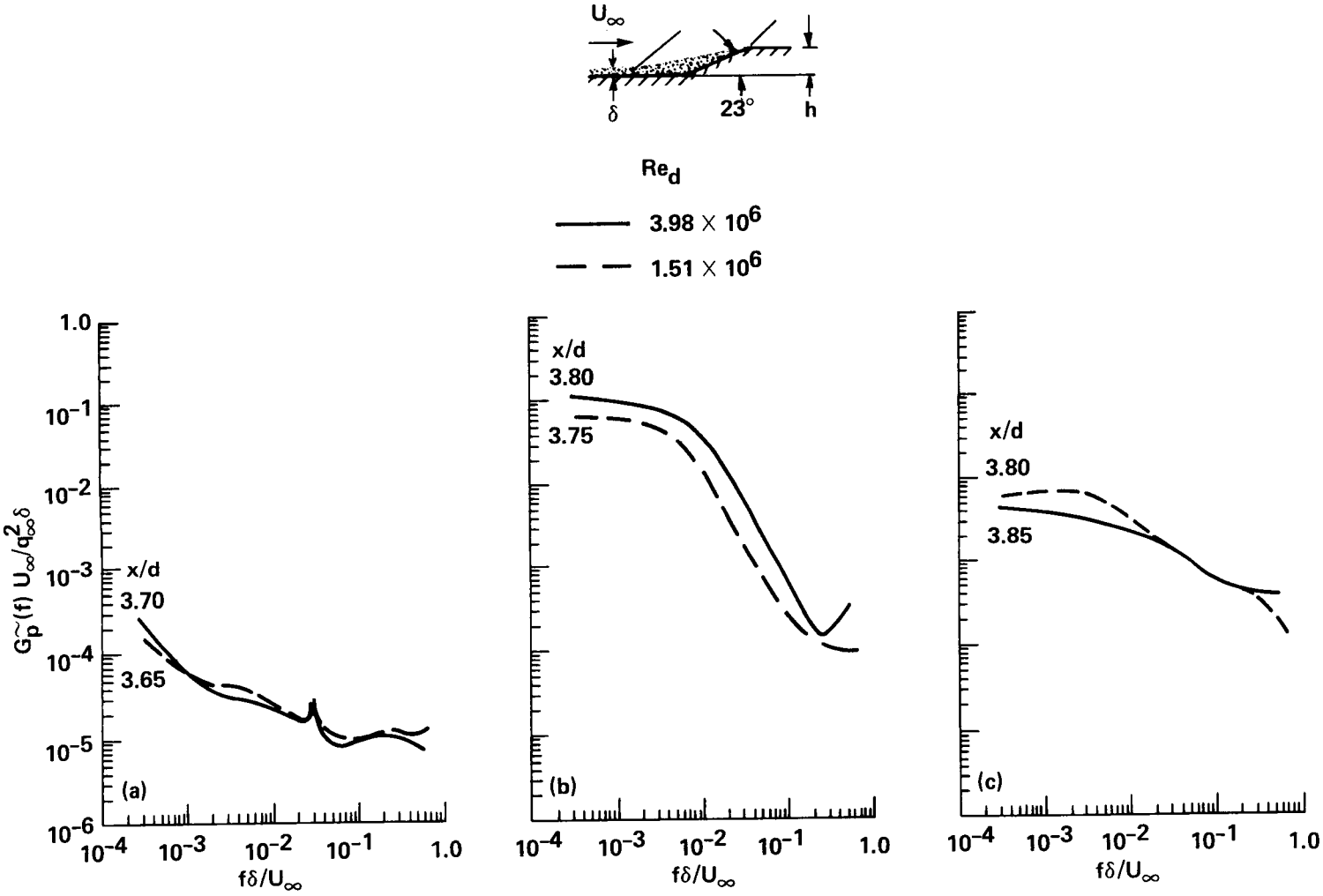

(a) Attached flow.

(b) Shock wave.

(c) Separated flow.

Figure 27.– Effect of Reynolds number on the power spectra of the pressure fluctuations in various flow regions ahead of the $\theta = 23^\circ$ cone frustum with no crossflow ($\alpha = 0^\circ$); $M_\infty = 2.0$; $s/d = -0.15$.

1. Report No.	2. Government Accession No.	3. Recipient's Catalog No.
NASA TP-1951		

4. Title and Subtitle	5. Report Date
CROSSFLOW EFFECTS ON STEADY AND FLUCTUATING PRESSURES ON AN OGIVE-CYLINDER CONE-FRUSTUM MODEL IN SUPERSONIC SEPARATED FLOW	November 1981
	6. Performing Organization Code
7. Author(s)	8. Performing Organization Report No.
Jules B. Dods, Jr., and Charles F. Coe	A-8563
	10. Work Unit No.
9. Performing Organization Name and Address	505-31-31
Ames Research Center, NASA, Moffett Field, Calif. 94035	11. Contract or Grant No.
	NAS2-10139
	13. Type of Report and Period Covered
12. Sponsoring Agency Name and Address	Technical Paper
National Aeronautics and Space Administration Washington, D.C. 20546	14. Sponsoring Agency Code

15. Supplementary Notes

Jules B. Dods, Jr.: Raman Aeronautics, Inc., Palo Alto, California.
Charles F. Coe: Ames Research Center, Moffett Field, California.

16. Abstract

Wind-tunnel tests were conducted on an ogive-cylinder model with two axisymmetric protuberances having cone frustum angles of $\theta = 23°$ and $45°$ that were used to generate detached shock waves and the resulting separated flow areas downstream of the shock. The tests were conducted in the Ames Research Center's 9- by 7-Foot Supersonic Wind Tunnel at a free-stream Mach number of 2.0 and at Reynolds numbers of 1.5×10^6 and 3.9×10^6, based on body diameter. The model had an afterbody fineness ratio of 8.3, and the ogive nose had a fineness ratio of 3.0.

The major purpose of the investigation was to measure two characteristics of the fluctuating pressures in surface vortex flows that result from the crossflow component, $U_\infty \sin \alpha$, in combination with changes in the longitudinal pressure gradient: (1) the broadband, rms-pressure coefficients and (2) the power spectral densities. Measurements are presented for various flow regions on the model such as the attached turbulent boundary layer, the detached frustum shock wave, and separated flow areas. The results indicated that the pressure fluctuations around or in the neighborhood of the foci of the vortex flows had broadband intensities and power spectral densities nearly identical to the levels previously measured in separated-flow regions at angles of attack of $0°$.

17. Key Words (Suggested by Author(s))		18. Distribution Statement
Fluctuating pressures	Boundary layers	Unclassified - Unlimited
Steady pressures	Oil-flow technique	
Structural dynamics		STAR Category – 02
Vortex flow		

19. Security Classif. (of this report)	20. Security Classif. (of this page)	21. No. of Pages	22. Price*
Unclassified	Unclassified	58	A04

*For sale by the National Technical Information Service, Springfield, Virginia 22161

NASA-Langley, 1981